POLITECNICO DI TORINO
Repository ISTITUZIONALE

La-based perovskites for autothermal reforming: In-situ electrical conductivity measurements and catalytic study

(Article begins on next page)

22 June 2024

La-based perovskites for autothermal reforming: *In-situ* electrical conductivity measurements and catalytic study

Melodj Dosa [a,1], Enrico Sartoretti [a], Alessandro Monteverde [a], Samir Bensaid [a], Ionel Popescu [b], Ioan-Cezar Marcu [c,*], Patrizia Frontera [d], Angela Malara [d], Anastasia Macario [e], Marco Piumetti [a,*]

[a] *Department of Applied Science and Technology, Politecnico di Torino, Corso Duca degli Abruzzi 24, 10129 Torino, Italy*
[b] *Laboratory of Chemical Technology and Catalysis, Division of Exact Sciences, Research Institute of the University of Bucharest, 90, Panduri Street, 050663 Bucharest, Romania*
[c] *Laboratory of Chemical Technology and Catalysis, Department of Inorganic and Organic Chemistry, Biochemistry and Catalysis, Faculty of Chemistry, University of Bucharest, 4-12, Blv. Regina Elisabeta, 030018 Bucharest, Romania*
[d] *Civil Engineering, Energy, Environmental and Materials Department, University Mediterranea of Reggio Calabria, 89134 Reggio Calabria, Italy*
[e] *Department of Environmental Engineering, University of Calabria, Cosenza 87036, Italy*

ARTICLE INFO

ABSTRACT

In this work, La-based perovskites with various stoichiometries were synthesized and tested for Autothermal Reforming (ATR) in the intermediate temperature solid oxide fuel cell technology (IT-SOFC). Three materials were compared, namely $La_{0.5}Sr_{0.5}Fe_{0.8}Cu_{0.2}O_{3-\delta}$ (LaSrFeCu), $La_{0.3}Sr_{0.7}Fe_{0.7}Ti_{0.3}O_{3-\delta}$ (LaSrFeTi) and $La_{0.4}Sr_{0.4}Ba_{0.2}TiO_{3+\delta}$ (LaSrBaTi), where the subscripts indicate the atomic ratio used during the synthesis. In the specific, two wet-chemistry approaches (solution combustion synthesis and chelate complex route) were used to obtain mesoporous La-based perovskites. The physico-chemical properties of the materials were analyzed by complementary techniques. Their semiconductive and redox properties were studied by *in situ* electrical conductivity measurements as a function of the temperature and, at constant temperature, as a function of the partial pressure of oxygen and of the nature of the gaseous atmosphere flowing over the solid. Then, the perovskites were impregnated with 7 wt% of Ni, characterized and tested for the autothermal reforming of ethanol, model biogas, and methane at 500 and 600 °C. Catalytic tests showed a high syngas production (83%) when ethanol was used as fuel at 600 °C. Analysis of the carbon deposited under different reaction conditions was also performed, in order to assess the stability of the proposed materials. Ni_LaSrBaTi exhibited almost complete ethanol conversion and high H_2 selectivity, together with strong structural/thermal stability and good resistance to coke formation, which make this catalyst a promising candidate as IT-SOFC's pre-layer anode.

1. Introduction

Solid Oxide Fuel Cells (SOFC) are devices able to generate electricity and heat through the electrochemical oxidation of different fuels (*i.e.*, biofuels or methane) and reduction of air, producing lower greenhouse emissions compared to internal combustion engines [1–3]. The most widely used SOFC's anode consists of Ni-YSZ material, which however presents some issues: deposition of carbon on the anode surface occurs during the cell operation, causing a decrease in the electrical conductivity and redistribution of temperature and current [4–9]. Despite the current limitations hindering SOFC commercialization, the growing demand for more efficient power generation systems is the driving force for the development of more cost-effective, non-toxic, stable, and carbon tolerant catalysts for the SOFC's anode.

One strategy to advance the SOFC commercialization is the reduction of the working temperature to 600–700 °C: the thermal degradation process, which allows the formation of coke on anode surface, is thereby decelerated [10,11]. The SOFC working under these temperature conditions are called Intermediate Temperature Solid Oxide Fuel Cells (IT-SOFC). On the other hand, another strategy can be the development of

---

new materials for SOFC's anode: in the specific, in the last years, several research groups have focused their attention on perovskite-based materials as valid alternatives to Ni-YSZ [12–17]. The reason of such an interest is due to their flexible composition: the general perovskites formula is ABX_3, where A and B are cations with total charge +6 and X can be fluoride, chloride, or, usually, oxide [10,15,16]. The A and B sites, which are 12-fold and 6-fold oxygen-coordinated holes, respectively, can be occupied by a large variety of cations allowing the formation of perovskite-related structure compounds [12,17,18]. Due to this feature, most of the perovskites' structures are distorted.

The improvement of the morphological properties of perovskites is a key point to obtaining IT-SOFC with better performances. Thus, the attention goes to mesoporous perovskite-based materials: the concentration of active sites is higher in mesoporous materials due to their high specific surface area. Furthermore, mesoporous materials are the right compromise between high surface area and pores diameter (2–50 nm), which improves the fluid-solid interactions and transport of the ionic and electronic charge carriers [14]. In the literature, various synthesis pathways and different chemical compositions of perovskites are reported, and the La-based ones are the most studied [15,19–22]. Several research groups synthesized perovskites through sol-gel [23], solid-state reaction [14,15], Solution Combustion Synthesis [21], and Chelate Complex Route [24].

The aim of this work is to study novel mesoporous La-based perovskites as pre-layer for anodes in IT-SOFC. Three different La-based perovskites, with different cations, were synthesized with various stoichiometries and then characterized by different techniques, to investigate their textural, structural, and chemical properties. The Solution Combustion Synthesis (SCS) and the Chelate Complex Route (CCR) were chosen as synthesis methods to obtain mesoporous perovskite-related structures. *In-situ* electrical conductivity measurements were performed in order to study their semiconductive and redox properties. Further, after impregnation with Nickel (7 wt%), the catalytic activity of the synthesized materials was tested towards the ATR reaction of ethanol (EtOH), model biogas and methane (CH_4) at 500 and 600 °C, in order to evaluate, at a laboratory scale, the behavior of such materials as possible candidates as IT-SOFC's pre-layer anode.

2. Materials and methods

2.1. Samples preparation

$La_{0.5}Sr_{0.5}Fe_{0.8}Cu_{0.2}O_{3-\delta}$, $La_{0.3}Sr_{0.7}Fe_{0.7}Ti_{0.3}O_{3-\delta}$ and $La_{0.4}Sr_{0.4}Ba_{0.2}TiO_{3+\delta}$ are the La-based perovskites synthesized in this work. The subscript indicated the atomic ratio used for the synthesis.

2.1.1. Solution combustion synthesis (SCS)

The $La_{0.5}Sr_{0.5}Fe_{0.8}Cu_{0.2}O_{3-\delta}$ sample was synthesized through the SCS method. The synthesis was adapted from references [21, 25]. Briefly, an aqueous solution, containing ultra-pure water and the metal precursors (as nitrates, provided by Sigma-Aldrich) in stoichiometric ratio (the subscripts indicate the at. % ratios) was prepared. The fuel-to-oxidizer ratio was fixed to 1.5 [25]. The glycine (provided by Sigma-Aldrich) was chosen as a fuel due to the right balance of surface area and crystallinity of the final products. After a few minutes of stirring, the resulting solution was transferred in a crucible, which was put in an oven and calcinated in air with a heating ramp of 5 °C min^{-1} and kept at a constant temperature of 600 °C for 2 h. The sample was labelled as "LaSrFeCu".

2.1.2. Chelate complex route (CCR)

The CCR is similar to SCS procedure and was adapted from reference [24]. In both synthesis methods the samples were placed into an oven to allow the formation of the final metal oxide powder. However, in the case of CCR, the reaction goes through a polycondensation process, which is not present in the SCS method. Specifically,

$La_{0.3}Sr_{0.7}Fe_{0.7}Ti_{0.3}O_{3-\delta}$ and $La_{0.4}Sr_{0.4}Ba_{0.2}TiO_{3+\delta}$ were synthesized with this method and labelled as LaSrFeTi and LaSrBaTi, respectively. Stoichiometric amount of titanium (IV) isopropoxide (Sigma-Aldrich) was added to glycerol (Sigma-Aldrich). After 30 min of stirring, citric acid (Sigma-Aldrich) was added. The resulting mixture was heated to 60 °C and stirred for 1 h. Afterward, stoichiometric amounts of metal nitrates (provided by Sigma-Aldrich) were added at 30 min intervals each, under continuous stirring. The solution was maintained at 60 °C for 2 h and then the temperature was raised to 130 °C to achieve polycondensation under vigorous stirring for other 2 h. The resulting gel was calcinated in air with a heating ramp of 2 °C min^{-1}. The first intermediate temperature (400 °C) was held for 2 h and the final temperature of 600 °C was kept constant for 2 h.

2.2. Samples impregnation procedure

The Ni-catalysts were prepared by the wetness impregnation procedure [26]. In the process, the permeable material is impregnated with a solution containing the desired substance (in this case Ni precursor), and subsequently the solvent is dried or evaporated, leaving the substance deposited within the material's pores. With this approach, it is possible to customize the impregnation by manipulating the concentration of the solution and the drying conditions, allowing to achieve desired qualities and functions in the resulting material. In this work, the metal source, nickel nitrate hexahydrate $Ni(NO_3)_2\cdot6H_2O$, supplied by Sigma-Aldrich and used with no further purification, was dissolved in ethanol solvent. This solution was used to impregnate, drop by drop, the perovskite supports; then the solvent was allowed to evaporate leaving the Ni precursor deposited within perovskites. The total metal loading was 7 wt% with respect to the support. After the impregnation, catalysts were dried at 120 °C, calcined at 600 °C for 4 h with a heating rate of 2 °C min^{-1} and then cooled down with a cooling rate of 2 °C min^{-1}. Finally, the activation of the catalysts was performed for 1 h at 750 °C under H_2 flow (10 vol% in He) using the same heating and cooling rates as above. Final catalysts were labelled as Ni_LaSrFeCu, Ni_LaSrFeTi and Ni_LaSrBaTi.

2.3. Samples characterization

The powder X-ray diffractograms (XRD) were recorded on a X'Pert Philips PW3040 diffractometer using Cu Kα radiation (2θ range = 20°–80°; step = 0.05° 2θ; time per step = 0.2 s). the Powder Data File database (PDF 2000, International Centre of Diffraction Data, Pennsylvania) was used for the index of the diffraction peaks. All the fresh as-prepared catalysts and Ni-catalysts (fresh and spent) were characterized by the XRD technique.

The specific surface area (S_{BET}) and the total pore volume (V_P) were determined *via* the N_2 physisorption analysis at −196 °C (Micromeritics ASAP 2020) on powders previously outgassed at 200 °C for 2 h to remove moisture/adsorbed water and atmospheric pollutants.

A field emission scanning electronic microscope (FESEM) (Zeiss Merlin, Gemini-II column, using an extra high tension (EHT) of 3 kV, a working distance (WD) of 2.8 mm and a probe intensity of 120 pA) was used to analyze the catalysts morphologies.

SEM-EDX technique was used to investigate fresh and spent Ni-catalysts. A Phenom Pro-X scanning electron microscope equipped with an energy-dispersive x-ray (EDX) spectrometer was utilized for this purpose. The EDX analysis was used to evaluate the content and dispersion of metals, by acquiring at least 20 points of investigation for three different magnifications for all samples [27].

Thermogravimetric TGA/DSC analysis (Netzsch, Selb, Germany) was used to investigate the carbon deposited over spent Ni-catalysts after reaction. The thermal analysis was carried out in the range 20–1000 °C with a heating rate of 2 °C min^{-1} under an air flow rate of 100 cm^3 min^{-1}.

Temperature-programmed reduction/desorption analyses were

realized in a ThermoQuest TPD/R/O 1100 analyzer, equipped with a thermal conductivity detector (TCD). The reducibility of the powder was studied by the H_2-TPR, in which a pre-treatment was carried out before the analysis by treating the sample with nitrogen (40 ml min^{-1}) at 500 °C for 1 h. In the H_2-TPR analysis, the catalyst was exposed to a reducing gas flow of 5 vol% H_2 in Ar (20 ml min^{-1}). The analysis was conducted under a programmed heating from 50 to 900 °C with a heating ramp of 10 °C min^{-1}. In the O_2-TPD analysis, the sample was initially pre-treated under a 10 vol% O_2 in He flow (50 ml min^{-1}) at 550 °C for 120 min and then cooled down to 50 °C still under the gas flow. Then, the TPD measurement was performed by heating the sample until 900 °C under a He flow (50 ml min^{-1}) at a constant heating rate (10 °C min^{-1}).

The X-ray photoelectron spectroscopy (XPS) measurements were performed on an XPS PHI 5000 Versa probe apparatus using the following conditions: band-pass energy of 187.85 eV, take-off angle of 45° and diameter of the X-ray spot of 100.0 μm. The curve-fitting was performed by CasaXPS 2.3 software. A Shirley type baseline was used for the deconvolution of high resolution XPS spectra of each element of interest.

Electrical conductivity measurements were carried out to study the semiconductive and redox properties of both perovskite supports and supported nickel catalysts. To ensure good electrical contacts between the catalyst grains, prior to the electrical conductivity measurements, the solid powders were compressed at *ca.* 2.76×10^7 Pa (4000 psi) using a Carver 4350.L pellet press. The densities of the pelletized samples are tabulated in Table 1.

The oxide pellet was tightened between two circular platinum electrodes placed in a horizontal quartz tube inserted in an electrical furnace. Pt—Rh thermocouples soldered to the electrodes were used to control the temperature. The flow rate of the gas stream passing over the samples was controlled by fine needle valves and was measured by capillary flow meters. The platinum electrodes were connected to a FLUKE 177 multimeter, which was set to ohmmeter and used to measure the electrical resistance of the pellet. This was converted into conductivity (σ, in ohm^{-1} cm^{-1}) by using the Eq. (1):

$$\sigma = 1/\rho = 1/R \times h/S \tag{1}$$

where ρ is the electrical resistivity of the solid (in ohm cm), R is the measured electrical resistance (in ohm), h is the thickness of the pelletized sample (between 2 and 3 mm) and S is the cross-section area of the circular platinum electrodes (whose diameter is 13 mm), *i.e.*, the contact area between the metallic conductor and the semiconducting oxide sample. The electrical conductivity of the pellet is proportional to the concentration of the main charge carriers, n, according to the Eq. (2) [28]:

$$\sigma = An \tag{2}$$

where A is the constant of proportionality that includes the charge of the electron, the mobility of the charge carriers and the number and quality of the contacts between the grains. Taking into consideration that the oxide samples have similar specific surface areas and were pelletized at the same pressure, and that the electrical conductivity measurements were standardized, the constant A can be considered similar for all the samples under identical conditions. Before the electrical conductivity

Table 1
Density of the pelletized Ni-free and Ni-bearing perovskite samples.

Ni-free perovskite sample	Pellet density (g cm^{-3})	Ni-bearing perovskite sample	Pellet density (g cm^{-3})
LaSrFeCu	2.73	Ni_LaSrFeCu	3.12
LaSrFeTi	2.64	Ni_LaSrFeTi	2.97
LaSrBaTi	2.48	Ni_LaSrBaTi	2.73

measurements, each sample was thermally treated in flowing air to 250 °C to remove any adsorbed impurities, then cooled down to *ca.* 100 °C and finally heated again to the desired temperature with a rate of 5 °C min^{-1}. In this way, the concentration of adsorbed ionic species like HO$^-$ or H_3O^+ that could be responsible for an additional surface conductivity is negligible. In this work, the common reference state for the variation of the electrical conductivity, both under different partial pressures of oxygen and under different gas streams, was fixed under air at 500 °C and atmospheric pressure. The different oxidizing and reducing gaseous atmospheres used are as follows: air – CH_4-air mixture (with 5 vol% CH_4) – air – H_2—Ar mixture (with 5 vol% H_2) – air.

2.4. Catalytic tests

The Autothermal Reforming (ATR) tests were performed with three different fuels: EtOH, model biogas and CH_4. The ATR reactions were performed at 500 and 600 °C adopting as operative conditions the ratios O/C = 0.5 and S/C = 2.5 where O is the oxygen, C is the carbon of the fuel (EtOH, model biogas, or CH_4) and S is the steam in the inlet stream. Catalytic activity experiments were performed at atmospheric pressure in a quartz microreactor (internal diameter = 4 mm) placed in a ceramic tube furnace, at a gas hourly space velocity (GHSV) of 120,000 h^{-1}. The catalyst (~50 mg) was placed between quartz wool in the middle of the reactor. The reaction temperature was monitored by a thermocouple inserted into the reactor bed through a quartz tube. The temperature of the reactor bed was kept constant by an electronic controller. The maximum deviation measured in the reactor bed from the nominal temperature was ~10 °C. An isocratic pump (Varian ProStar 210, Varian Inc., Palo Alto, California, CA, USA) connected to an evaporator that was heated at 220 °C, was used to feed water in the gas stream and to control the steam to carbon ratio (S/C) in the reaction gas mixture; N_2 was used as internal standard. The gas lines were heated at 120 °C to prevent condensation. The microreactor was operated in down-flow mode with the gas inlet placed at the top of the reactor. Reaction products were analyzed with an on-line gas chromatograph (GC Agilent 6590, Agilent, Santa Clara, CA, USA) equipped with FID, FPD and TCD detectors and four columns (Alumina, Porapak Q, Haysep, Molecular Sieves (MS 5A)), for their separation and detection. The catalytic activity results were generally taken 20 min after the reaction conditioning and reproducible data were obtained for registration periods of at least 600 min repeated three times. Overall carbon and H_2 balances were close to 100% in each experiment with moderate standard deviation lower than 3 [29].

3. Results and discussion

3.1. Textural and structural properties

The XRD was used to investigate the crystalline structure of the as-prepared samples. The results are reported in Fig. 1. The LaSrBaTi sample shows the XRD pattern of La$_{0.4}$Sr$_{0.4}$Ba$_{0.2}$Ti$_{0.8}$O$_{3+\delta}$ perovskite (pdf nr. 04–015–2708), exhibiting the typical (100), (110), (111), (200), (210), (211), (220) and (310) crystal planes. The LaSrFeCu and LaSrFeTi patterns can be ascribed to Sr$_{0.2}$Cu$_{0.05}$La$_{0.8}$Fe$_{0.95}$O$_3$ (pdf nr. 04–019–6593) and Sr$_{0.5}$La$_{0.5}$Fe$_{0.5}$Ti$_{0.5}$O$_3$ (pdf nr. 04–002–9185), respectively. For both samples, diffraction lines corresponding to SrCO$_3$ pattern (pdf nr. 04–006–5445) were also detected, meaning that the amount of Sr inside the perovskite structure is likely lower compared with the theoretical value adopted for the synthesis, due to the formation of SrCO$_3$. A similar observation can be made for copper in LaSrFeCu, since a low-intensity reflection of CuO was detected in the XRD profile of this sample. These non-uniformities, which may be related to the calcination temperature, enhance the charge carrier transport properties and, hence, overall conductivity of perovskite materials. As known, the conductivity may be impacted by non-uniformity or changes in perovskite phases in different ways. i) Crystal lattice imperfections like missing atoms or altered atoms can form electron or hole carriers. These
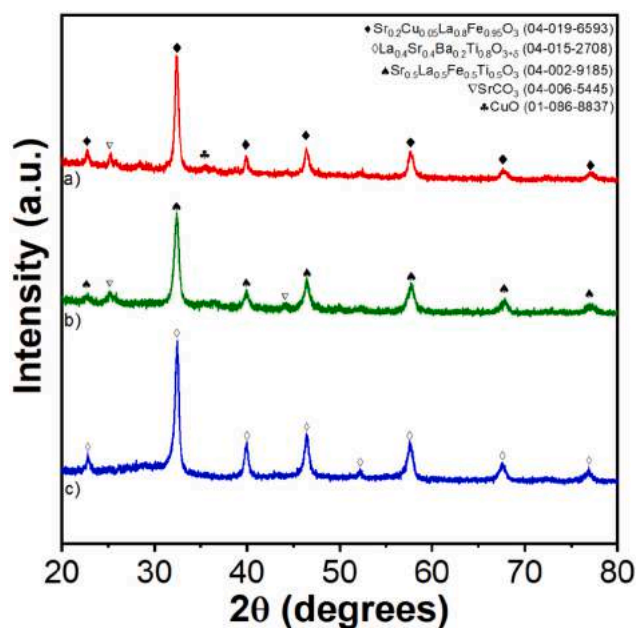
Fig. 1. X-ray diffractograms of a) LaSrFeCu, b) LaSrFeTi and c) LaSrBaTi.

imperfections can function as charge carriers or affect charge carrier movement, influencing conductivity. ii) Perovskites have grains with distinct orientations or phases, and higher or lower conductivity can result from grain boundaries and contacts between phases. Charge carriers can pass through or be blocked by these contacts, impacting material conductivity. iii) Changing the perovskite's composition or adding components might cause localized conductive areas. Doping with certain elements adds charge carriers, improving conductivity [30].

Fig. 2 reports the XRD patterns of the samples impregnated with Ni, before the activation (labelled as "Ni_LaSrFeCu (wi)", "Ni_LaSrFeTi (wi)" and "Ni_LaSrBaTi (wi)") and after the activation. Nickel was mainly present as NiO_2 after impregnation, eventually becoming metallic Ni during reduction. Ni particles are likely larger in the Ni_LaSrFeCu and Ni_LaSrFeTi samples, which are characterized by sharper Ni XRD peaks; this is consistent with the EDX maps of these two materials, in which more intense colored areas ascribable to bigger Ni clusters can be observed (Fig. 2). Concerning the perovskite lattice, the Ni_LaSrBaTi catalyst completely retained its crystalline structure after activation, as confirmed by its almost unchanged XRD pattern. Conversely, Ni_LaSrFeCu and Ni_LaSrFeTi exhibited important changes after the activation treatment, compared to their non-activated counterparts. In detail, high temperature reduction induced the formation of a strontium-iron mixed oxide in both the samples, and it also resulted in sintering; the XRD peaks corresponding to the perovskite structure are indeed sharper after activation, signaling that growth and aggregation of crystallites have occurred, especially in the case of Ni_LaSrFeCu. A more marked phase transformation is likely associated to reduced surface area, favoring Ni aggregation. Unfortunately, the overlapping of multiple XRD peaks does not allow a reliable numerical estimation of the average crystal size in perovskites and in the Ni particles after activation. Segregation of metallic iron or copper could also have occurred, although the typical peaks of these metals cannot be clearly identified since they are overlapped with those of the other species. The reason for such different behaviors is related to the chemical composition of the perovskites.

In fact, the only reducible element in LaSrBaTi is titanium, while the other two samples also contain copper and iron cations, both of which have two stable oxidation states, *i.e.*, Cu^{2+} and Cu^+, and Fe^{3+} and Fe^{2+}, respectively. Moreover, Cu and Fe can be easily reduced to the metallic form, in contrast to Ti (as also confirmed by H_2-TPR and XPS, see below).

Thus, the structure of the Ni_LaSrFeCu and Ni_LaSrFeTi samples can be expected to be majorly affected by a thermal treatment in reducing atmosphere, also considering that temperature is one of the main drivers for perovskite decomposition.

The N_2 physisorption was used to investigate the surface area and the total pore volume of the samples. The results are reported in Table 2 while the adsorption isotherms are displayed in Fig. S1.

LaSrFeTi and LaSrFeCu exhibited type IV isotherms with clear H3 hysteresis loops, corresponding to an interparticle porosity. LaSrBaTi showed a type IV isotherm too, but with a more complex hysteresis loop, which is a combination of H2b and H3 types and corresponds to an interparticle porosity with pore blocking in a wide range of pore necks [31]. The BET specific surface areas (S_{BET}) of the perovskite samples are relatively low and in agreement with the literature data [21,24,25]. Thus, depending on the sample composition, they vary from 12 m^2 g^{-1} for LaSrFeCu to 38 m^2 g^{-1} for LaSrBaTi. The perovskites also show the presence of porosity, with total pore volume in the range 0.07–0.21 cm^3 g^{-1}. The pore size distribution was evaluated, and the average pore dimensions are in the range of mesoporous materials, as shown in Fig. S2 (LaSrFeCu = 11 nm, LaSrFeTi = 11 nm, and LaSrBaTi = 10 nm). It is interesting to point out that the LaSrBaTi sample shows an increase in the pore volume for pore sizes higher than 1000 Å. This suggests that this material has a larger mesopore structure compared to the other two perovskites, which explains the higher S_{BET} obtained.

The morphology of the samples was investigated by FESEM analysis, and representative images are reported in Fig. 3. All the samples display foam-like morphology, which is characteristic of the two synthesis methods used [21,24,25,32,33]. However, the SCS-synthesized sample (LaSrFeCu) shows larger and rather flat aggregates, in contrast to the finer nanoparticles observed in the two perovskites prepared by CCR. Among the latter materials, LaSrBaTi has a better-developed three-dimensional structure which allows higher surface area compared to LaSrFeCu and LaSrFeTi, in agreement with the N_2 physisorption results.

3.2. Chemical properties

The H_2-TPR analysis was performed in order to investigate the reducibility of the samples, the results obtained being reported in Fig. 4A. The LaSrFeTi sample exhibits peaks between 400 and 650 °C, which can be assigned to the gradual reduction of Fe^{3+} to Fe^{2+} [24,34].

At higher temperatures (above 650 °C), the initial reduction of Ti^{4+} can occur alongside the reduction of Fe^{2+} to Fe^0 [24]. At 900 °C, the reduction of Ti^{4+} species in the bulk begins [24]. The LaSrBaTi sample shows the reduction of Ti^{4+} in the range between 700 and 900 °C [24]: the first peak (735 °C) is attributed to the reduction of the surface Ti^{4+} species, while the peak at high temperature (875 °C) to the bulk Ti^{4+} reduction. The insertion of Ba allows the reduction of Ti^{4+} at a lower temperature (875 °C) in this sample [19]. For this reason, in LaSrBaTi sample, there is no peak centered at 900 °C which, on the other hand, occurs in the LaSrFeTi sample. The LaSrFeCu sample shows a peak at 223 °C, which can be assigned to the copper reduction from Cu^{2+} to Cu^0 [32,35]. The peaks below 600 °C can be assigned to the gradual reduction of Fe^{3+} or Fe^{2+} species [34]. Instead, the peak at higher temperatures is attributed to the reduction of Fe^{3+} or Fe^{2+} to Fe^0 [34]. H_2-TPR analysis evidenced that the LaSrFeCu sample is able to reduce at lower temperatures, comparing with the other two samples.

O_2-TPD analysis was performed in order to evaluate the oxygen desorption capacities of the studied samples. Fig. 4B reports the O_2-desorption profiles. As a whole, the several peaks of these samples could be ascribed to the releases of oxygen by the different oxide-phases evidenced in the XRD analysis. Usually, four types of oxygen can be evidenced during O_2-TPD tests over La-based perovskites: physically adsorbed oxygen (< 100 °C), superoxide species (100–300 °C), monatomic oxygen (400–550 °C), and lattice oxygen (>550 °C) [36]. The LaSrFeTi sample has a release of oxygen at lower temperature (233 °C) compared to the other two materials, which can be ascribed to
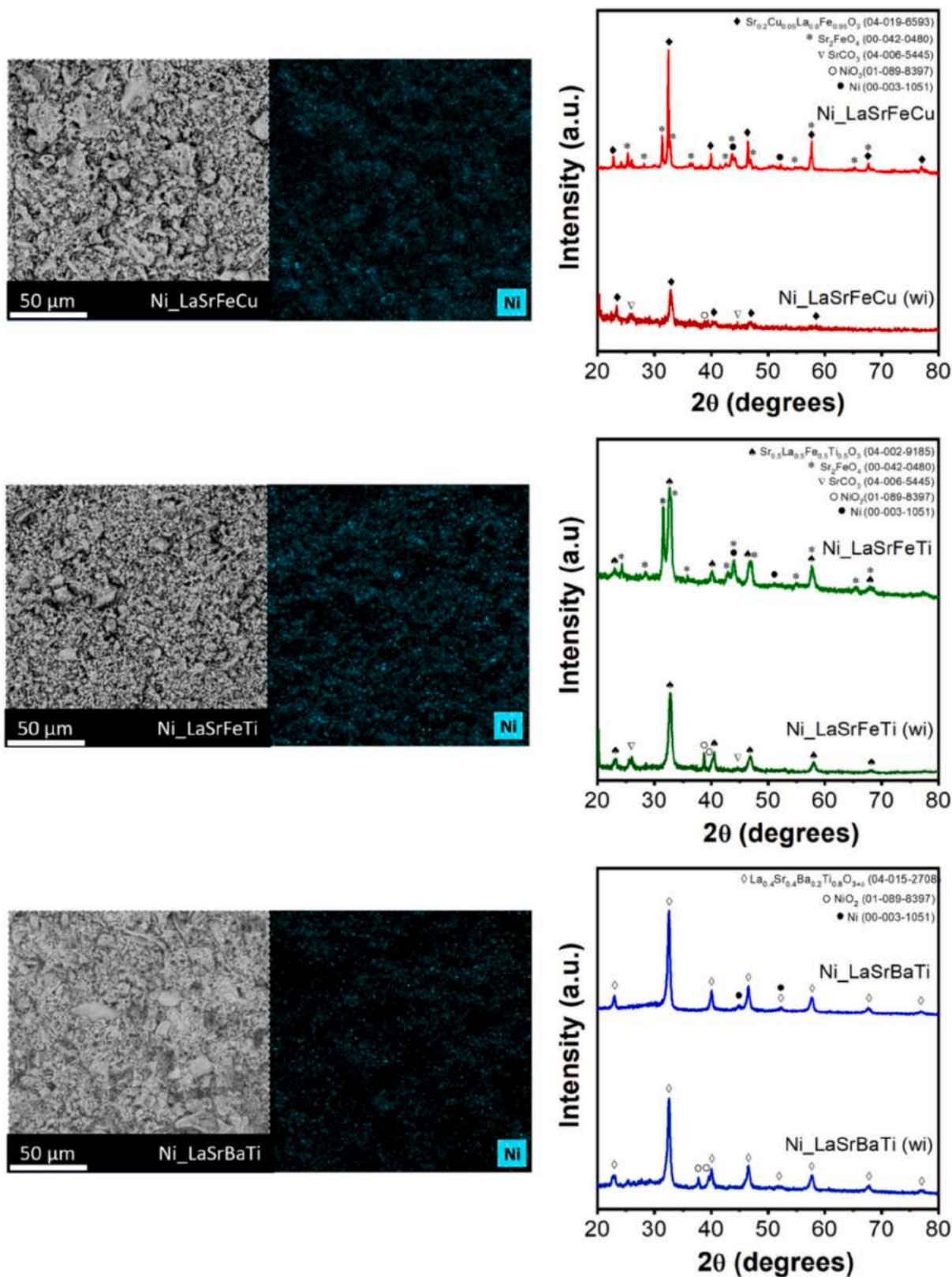
Fig. 2. SEM-EDX and XRD analysis. Ni_LaSrFeCu (wi), Ni_LaSrFeTi (wi) and Ni_LaSrBaTi (wi) are the sample impregnated with Ni before the activation. Ni_LaSrFeCu, Ni_LaSrFeTi and Ni_LaSrBaTi are the final catalysts.

Table 2

N$_2$ physisorption results evaluated at −196 °C.

Sample	S$_{BET}$[a] (m^{2}g^{-1})	V$_p$[b] (cm^{3}g^{-1})
LaSrFeCu	12	0.07
LaSrFeTi	35	0.21
LaSrBaTi	38	0.11

[a] Specific surface area was evaluated by the Brunauer–Emmett–Teller (BET) method.

[b] The total pore volume was evaluated by the Barrett-Joyner-Halenda (BJH) method during the desorption phase.

superoxide species on the surface of the materials [36]. All the three perovskites are then characterized by the release of bulk oxygen at high temperatures (>500 °C).

The XPS analysis was performed in order to investigate the oxidation state of the elements of interest and the surface species of the samples. Fig. 5 reports the deconvolution of high resolution XPS spectra of the elements of interest: O *1s*, Sr *3d*, La *3d* and Fe *3p* core levels. The average amounts of the elements derived from the XPS spectra deconvolution are reported in Table 3. The O *1s* spectra are depicted in Fig. 5A. As a whole, for all the samples, the peaks in the range 528.5–529.5 eV can be attributed to lattice oxygen (O$_\beta$). On the other hand, at higher binding energy (530.0–535.0 eV), the peaks can be assigned to the chemisorbed oxygen (O$_\alpha$) related to adsorbed oxygen and water, carbonates as well as hydroxyls species [25,32,37–41]. The average quantities are reported in Table 3, in terms of O$_\alpha$/O$_\beta$. Fig. 5B reports the Sr *3d* spectra, which show

two peaks, Sr 3d$_{5/2}$ and Sr 3d$_{3/2}$, due to the spin-orbit coupling. By the Sr *3d* core level deconvolution, the average amount of SrCO$_3$ and SrO species can be investigated (values reported in Table 3) [42,43]. Notably, all the samples contain SrCO$_3$ at their surface, in agreement with the XRD results (*vide supra*). The LaSrBaTi sample exhibits the lowest amount of strontium carbonate, which indeed was not detected by XRD. The La *3d* region (Fig. 5C) shows two doublets at 835 and 852 eV that can be attributed to two spin-orbit couplings of La 3d$_{5/2}$ and La 3d$_{3/2}$, respectively. The magnitude of the multiplet split is diagnostic, a gap of 4.6 eV being related to La$_2$O$_3$ species, 3.9 eV to La(OH)$_3$ species and 3.5 eV to La$_2$(CO$_3$)$_3$ [20,44]. The relative abundance of these species is reported in Table 3. The Fe *2p* spectra are reported in Fig. 5D where three major peaks can be found: the low binding energy peak at 710 eV can be assigned to Fe 2p$_{3/2}$, the high binding energy peak at 723 eV corresponds to Fe 2p$_{1/2}$, and the small peak at 718 eV is the Fe 2p$_{3/2}$ satellite. The band at 710 eV can be deconvoluted into two peaks, one at 710 eV characteristic of Fe^{2+} and the other one at 711 eV related to Fe^{3+} oxidation state [45,46]. It is possible to calculate the average amount of these two species; the Fe^{2+}/Fe^{3+} values are reported in Table 3. It can be observed that the surface Fe^{2+}/Fe^{3+} ratio is higher for LaSrFeCu compared to LaSrFeTi. The Ti *2p* is characterized by a doublet assigned to Ti 2p$_{1/2}$ and Ti 2p$_{3/2}$, located at binding energies of 463 and 457 eV, respectively (Fig. S3, supporting information section) [47,48].

It is possible to discriminate the titanium oxidation state, namely Ti^{4+} or Ti^{3+}, by the Ti 2p$_{3/2}$ deconvolution. The surface Ti^{3+}/Ti^{4+} ratio is reported in Table 3. Interestingly, the LaSrFeTi shows a significantly
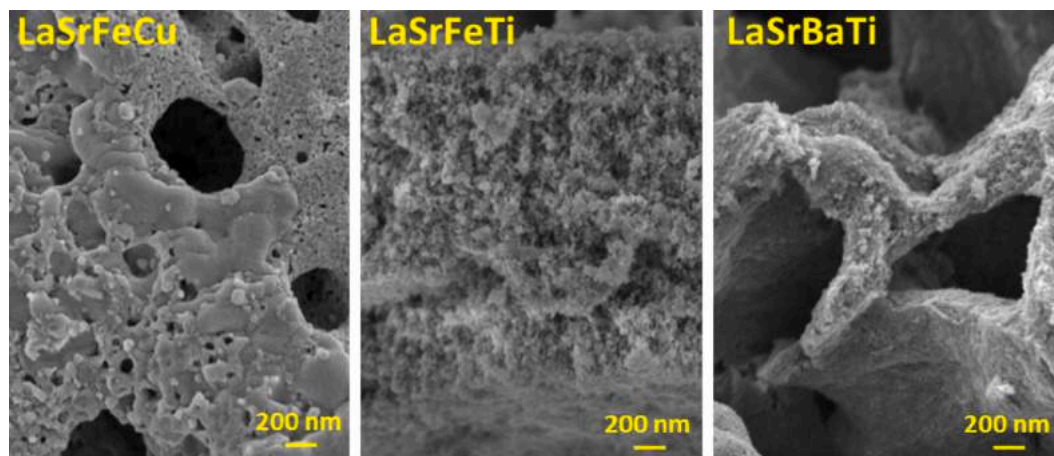

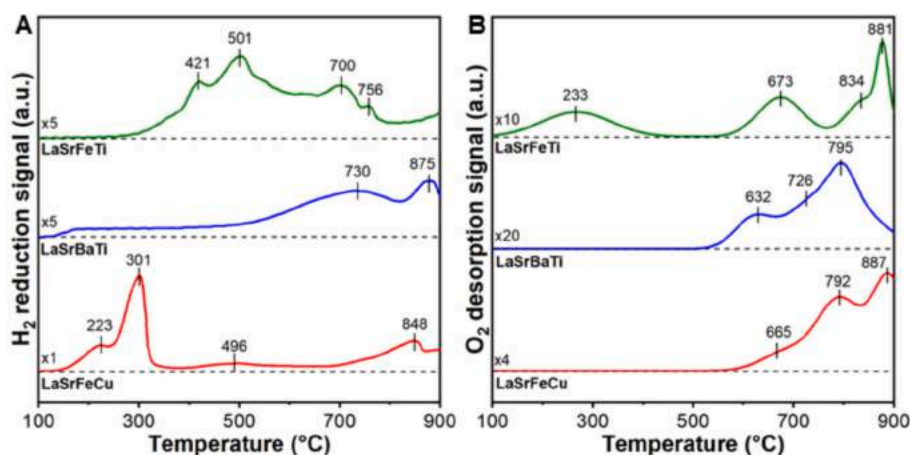**Fig. 3.** FESEM images of the samples.

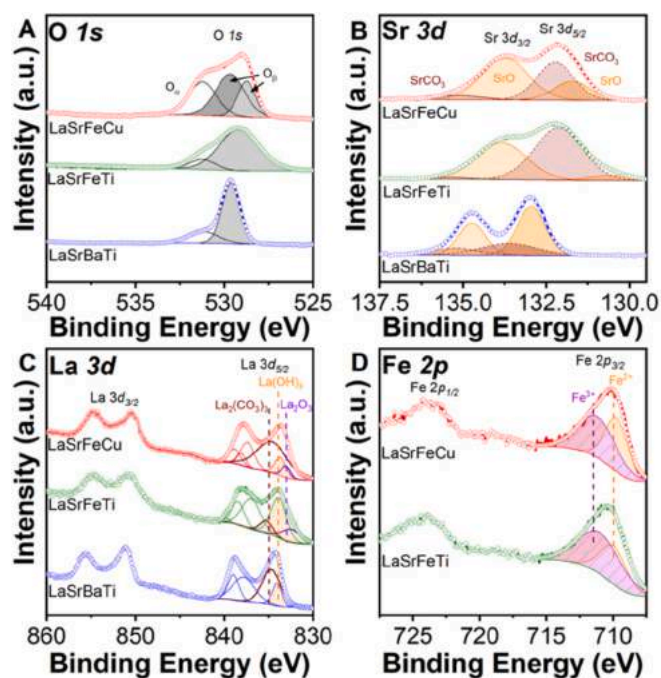**Fig. 4.** H$_2$-TPR (A) and O$_2$-TPD (B) profiles of the samples.

Fig. 5. XPS spectra of A) O 1*s*, B) Sr 3*d*, C) La 3*d* and D) Fe 2*p* core levels.

Table 3
Elemental compositions (at. %) of the samples as derived from the XPS spectra deconvolution.

Element		*LaSrFeTi*	*LaSrBaTi*	*LaSrFeCu*
O	O_α/O_β	0.17	0.34	0.50
Sr	SrO	0.44	0.69	0.63
	$SrCO_3$	0.56	0.31	0.38
La	La_2O_3	0.42	–	0.23
	$La(OH)_3$	0.48	0.45	0.17
	$La_2(CO_3)_3$	0.10	0.56	0.60
Fe	Fe^{2+}/Fe^{3+}	0.55	–	0.79
Ti	Ti^{3+}/Ti^{4+}	1.84	0.05	–

higher Ti^{3+}/Ti^{4+} ratio compared to LaSrBaTi. For the sake of brevity, the Cu 2*p* and Ba 3*d* XPS spectra are not shown. In fact, due to their lower concentration compared to the other elements, their characteristic XPS peaks have low intensity and, hence, it is difficult to observe and analyze them properly.

To better understand the effect of the reduction temperature on the perovskites and on their structure, further XPS measurements were performed on reduced LaSrBaTi, LaSrFeCu and LaSrFeTi (obtained by performing the same thermal treatment adopted for the activation of the impregnated catalysts). The results are reported in Fig. S4 and the average amount of the element of interest, namely O, Fe and Ti, are reported in Table S1. As previously mentioned in section 3.1, the reducing treatment at high temperature entails the reduction of different elements in the perovskites. It is possible to highlight this aspect by evaluating the surface Fe^{2+} to Fe^{3+} ratio, which significantly increases for both LaSrFeCu and LaSrFeTi. The latter sample also exhibits a partial reduction of titanium from Ti^{4+} to Ti^{3+} (Table S1). Moreover, the amount of surface oxygen species remarkably increases in these two perovskites as well. This indicates that the reducing thermal treatment can cause a deep change in the oxidation state of these samples, as also confirmed by H_2-TPR profiles; for this reason, after the reduction, the structure of the material changed, as previously mentioned and discussed in section 3.1 (Fig. 2). On the other hand, LaSrBaTi only exhibited an increase in the amount of surface oxygen, while the relative abundance of Ti^{3+} and Ti^{4+} remained constant, and rather low, after the

reduction. Thus, LaSrBaTi retained its crystalline structure after the reducing treatment because the oxidation state of the elements in the perovskite framework did not change significantly.

3.3. Materials characterization by electrical conductivity measurements

3.3.1. Electrical conductivity measurements as a function of temperature

The electrical conductivities of the perovskite-based mixed oxides, *i. e.*, LaSrFeCu, LaSrFeTi, and LaSrBaTi, have been measured as a function of temperature between 200 and 580 °C under air at atmospheric pressure. The variations of $\log(\sigma)$ *versus* temperature are compared in Fig. 6.

It can be observed that the electrical conductivity of the perovskite samples varies within a wide range, *i.e.*, seven orders of magnitude. Over the entire temperature range studied, it follows the order: LaSrBaTi < LaSrFeTi < LaSrFeCu, the LaSrBaTi sample showing measurable conductivity values starting from 220 °C. In Fig. 6 it can also be observed that the addition of Ni changes the electrical conductivity of the LaSrFeCu and LaSrFeTi samples. Thus, the conductivity of Ni-bearing LaSrFeCu decreases, while that of the Ni-bearing LaSrFeTi increases compared to their Ni-free counterparts, so that their conductivities become comparable. At the same time, the conductivity of the LaSrBaTi sample is not significantly affected by the presence of Ni. However, the Ni_LaSrBaTi sample shows measurable electrical conductivity values at temperatures higher than 280 °C. The order of conductivity of the Ni-bearing samples within the temperature range studied is as follows: Ni_LaSrBaTi << Ni_LaSrFeTi ≈ Ni_LaSrFeCu.

The Arrhenius plots ($\log(\sigma)$ *vs* reciprocal temperature) obtained for both Ni-free and Ni-bearing perovskite-based oxides are presented in Fig. 7, and their corresponding Arrhenius parameters are tabulated in Table 4.

In Fig. 7 it can be observed that all the samples show linear variations of $\log(\sigma)$ with the reciprocal temperature with at least two inflection points within the temperature range studied, except for Ni_LaSrFeTi which shows no inflection point. These linear variations are in agreement with a semiconducting behavior of all samples, with their electrical conductivity governed by the Arrhenius law (Eq. (3)):
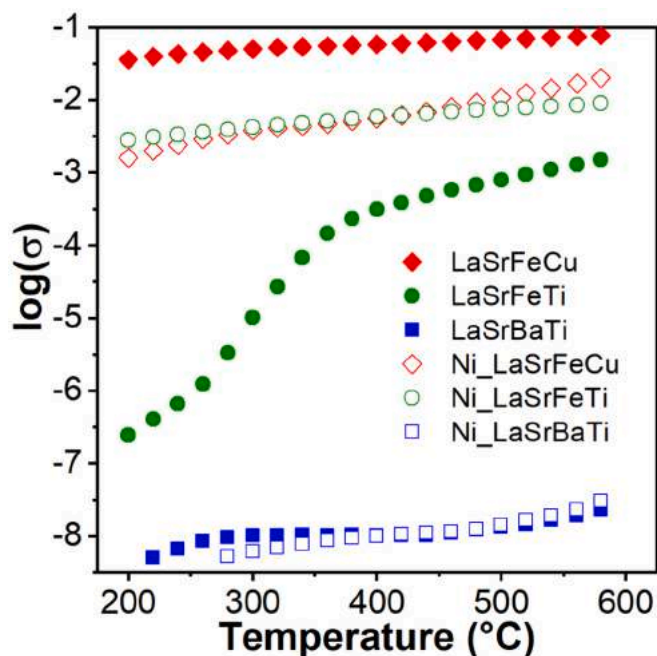

Fig. 6. Variation of $\log(\sigma)$ (σ in ohm^{-1} cm^{-1}) *versus* temperature for the Ni-free and Ni-bearing perovskite-based oxides under air.
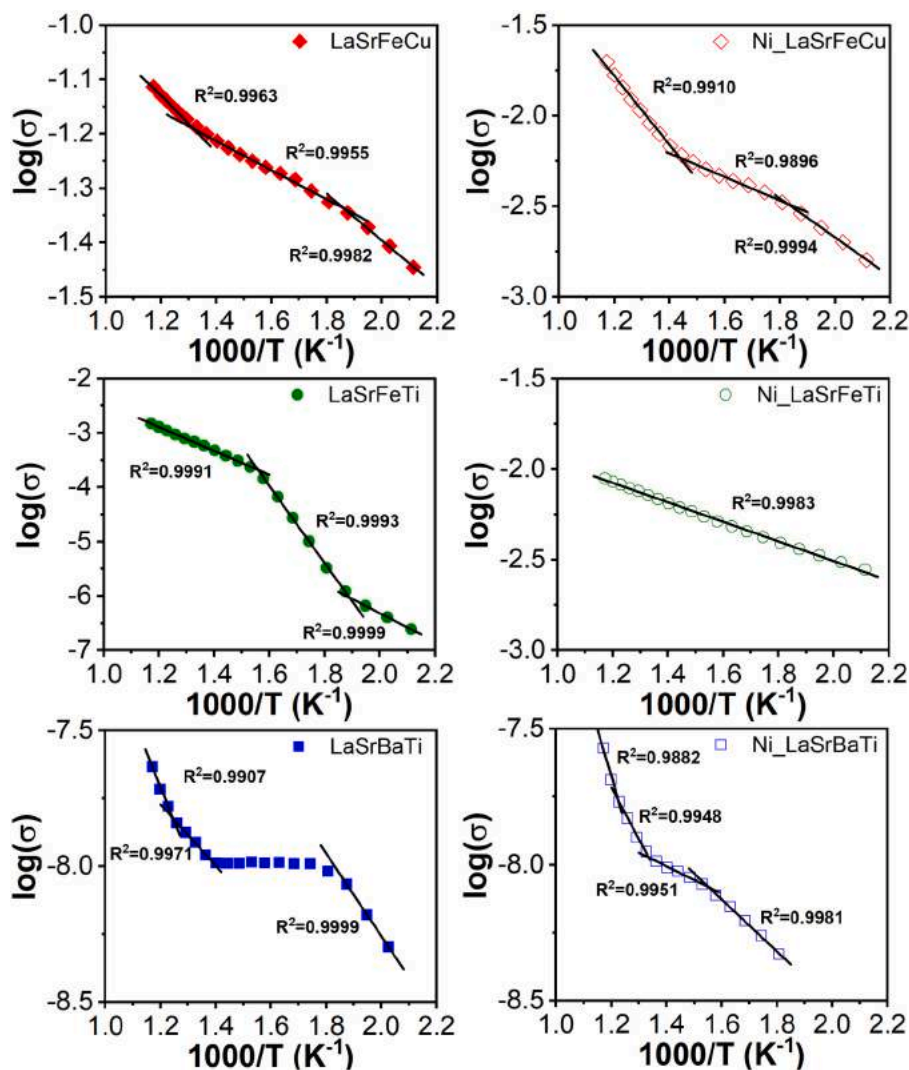
Fig. 7. Arrhenius plots for the electrical conductivity σ (in ohm^{-1} cm^{-1}) of the Ni-free and Ni-bearing perovskite-based oxides under air within the temperature range 200–580 °C.

$$\sigma = \sigma_0 \cdot exp[- E_c/(RT)] \tag{3}$$

where σ_0 is the pre-exponential factor and E_c is the activation energy of conduction. At the same time, the inflection points of the Arrhenius-type plots account for a change of the activation energy of conduction ascribed to changes in the conduction mechanism with temperature. The corresponding activation energies of conduction are tabulated in Table 4; all the values fall within the range observed for similar perovskite materials [49,50], accounting for the activation of the electrical mobility in a small polaron hopping mechanism. The only exception is represented by the significantly higher activation energy of conduction of the Ni-free LaSrFeTi sample in the intermediate temperature range, which rather corresponds to the charge carrier generation than to the activation of the electrical mobility. Notably, for the LaSrBaTi perovskite a temperature-independent behavior of the electrical conductivity is observed in the temperature range from *ca.* 290 to 440 °C. This behavior, which disappears in the Ni_LaSrBaTi sample, results from the neutralization of positive holes and electrons and will be better explained in the section 3.3.2.

Finally, the pre-exponential factor σ_0 in Eq. (3), which is a material constant depending on the concentration of the charge carriers, was estimated for all the samples from the intercept of the corresponding straight lines in Fig. 7. The values obtained for the different temperature ranges are listed in Table 4. It can be observed that σ_0 and, hence, the

Table 4

Arrhenius parameters of the electrical conductivity of the Ni-free and Ni-bearing perovskite-based oxides within different temperature ranges determined by the inflection points of the Arrhenius-type plots represented in Fig. 7.

Sample	E_c (eV)			σ_0 (Ω^{-1} cm^{-1})		
	Temperature range			Temperature range		
	Low	Intermediate	High	Low	Intermediate	High
LaSrFeCu	0.08	0.05	0.09	0.28	0.15	0.27
LaSrFeTi	0.52	1.42	0.44	0.08	2.6×10^7	0.55
LaSrBaTi	0.30	0[a] and 0.23[b]	0.51	6.0×10^{-6}	1.0×10^{-8} [a] and 3.8×10^{-7} [b]	2.2×10^{-5}
Ni_LaSrFeCu	0.22	0.13	0.38	0.30	0.05	3.22
Ni_LaSrFeTi	0.11	0.11	0.11	0.04	0.04	0.04
Ni_LaSrBaTi	0.19	0.10[c] and 0.38[d]	0.68	2.5×10^{-7}	5.0×10^{-8} [c] and 3.7×10^{-6} [d]	2.7×10^{-4}

[a] Temperature range from *ca.* 290 to 440 °C.
[b] Between 440 and 520 °C.
[c] Between 360 and 460 °C.
[d] Between 460 and 520 °C.

concentration of the charge carriers significantly depends on the nature of the material and, for a given solid, on the temperature. It is noteworthy that the addition of Ni to the LaSrFeCu oxide leads to an increase of the activation energy of conduction within all the temperature ranges determined by the different inflection points of the Arrhenius plot. Also, while the σ_0 value in the low temperature range is not much affected, it is three times lower for the Ni-bearing sample compared to Ni-free LaSrFeCu oxide in the intermediate temperature range, whereas it is more than ten times higher for the Ni_LaSrFeCu sample in the high temperature range. In the case of LaSrFeTi oxide, the addition of Ni leads to a unique activation energy of conduction within all the temperature range studied, which is significantly lower compared to the E_c values obtained for the Ni-free sample. At the same time, the σ_0 value is lower for the Ni_LaSrFeTi sample compared to the Ni-free LaSrFeTi oxide, a decrease by *ca.* nine orders of magnitude being noticed for the intermediate temperature range. The activation energy of conduction for the Ni_LaSrBaTi sample is lower than that of Ni-free LaSrBaTi oxide in the low temperature range, while in the intermediate and high temperature ranges, it is higher. At the same time, the σ_0 value is lower for the Ni_LaSrBaTi sample compared to the Ni-free LaSrBaTi in the low temperature range, while it is higher in the intermediate and high temperature ranges.

In summary, the addition of Ni to the multicationic perovskite oxides strongly impacts on their semiconducting behavior as a function of temperature; the observed effects are determined by the cationic composition of the oxide and, for a given composition, by the temperature range.

3.3.2. Electrical conductivity measurements as a function of the partial pressure of oxygen

To determine the dominant conduction mechanism of both Ni-free and Ni-bearing semiconducting oxides, the variation of their total conductivity was recorded as a function of the partial pressure of oxygen at constant temperature of 500 °C [51]. The results obtained are shown in log–log plots in Fig. 8. It can be observed that, except for LaSrBaTi, the two other perovskites show positive slopes, *i.e.,* $\partial\sigma/\partial P_{O2} > 0$, which correspond to a *p*-type behavior. Since the perovskite structure does not accept interstitial oxygen species [52], the main point defects in the *p*-type LaSrFeCu and LaSrFeTi perovskites are lanthanum vacancies, V_{La}''', together with substitutional defects of Sr(II) sitting on La(III) lattice points (the A sites in the ABO_3 perovskite structure), *i.e.,* Sr_{La}', and substitutional defects of Cu(II) or Cu(III) and Ti(III) or Ti(IV) sitting on Fe(III) lattice points (the B sites in the ABO_3 perovskite structure), *i.e.,* Cu_{Fe}' or Cu_{Fe}^x and Ti_{Fe}^x or $Ti_{Fe}^\bullet$, respectively. All the negatively charged defects are compensated by positively charged ones, such as $Fe_{Fe}^\bullet$, *i.e.,* Fe(IV) sitting on Fe(III) lattice points, and, for LaSrFeTi, $Ti_{Fe}^\bullet$ as well, which are associated to the positive holes, $h^\bullet$, responsible for the observed *p*-type behavior of these materials.

The oxidation of Fe(III) to Fe(IV) to compensate the charge imbalance due to the Sr(II) substitution for La(III) is in agreement with the results reported by Barbero et al. [53] for $La_{1-x}Ca_xFeO_3$ with $x < 0.2$. At the same time, as shown for x values higher than 0.2 in $La_{1-x}Ca_xFeO_3$ [53] or as low as 0.1 in $La_{1-x}Ca_xFe_{1-y}Ni_yO_3$ [54] and in line with the O_2-TPD data of our samples (Fig. 4), the creation of oxygen vacancies, $V_O^{\bullet\bullet}$, as charge compensating defects cannot be completely ruled out, mainly in the case of LaSrFeTi system for which the oxygen release was detected during the TPD process at temperatures significantly lower than 500 °C. However, because both LaSrFeCu and LaSrFeTi perovskites behave as *p*-type semiconductors, the charge compensating defects, such as $Fe_{Fe}^\bullet$, and $Ti_{Fe}^\bullet$ (for LaSrFeTi), are dominant.

The addition of Ni to the *p*-type LaSrFeCu and LaSrFeTi perovskites does not change the nature of the conductivity, as the slopes of the log(σ) – log(P_{O2}) plots remain positive (Fig. 8). However, interestingly, the *p*-type conductivity of the LaSrFeCu system decreases, while that of the LaSrFeTi increases in the presence of Ni. In other words, the deposition
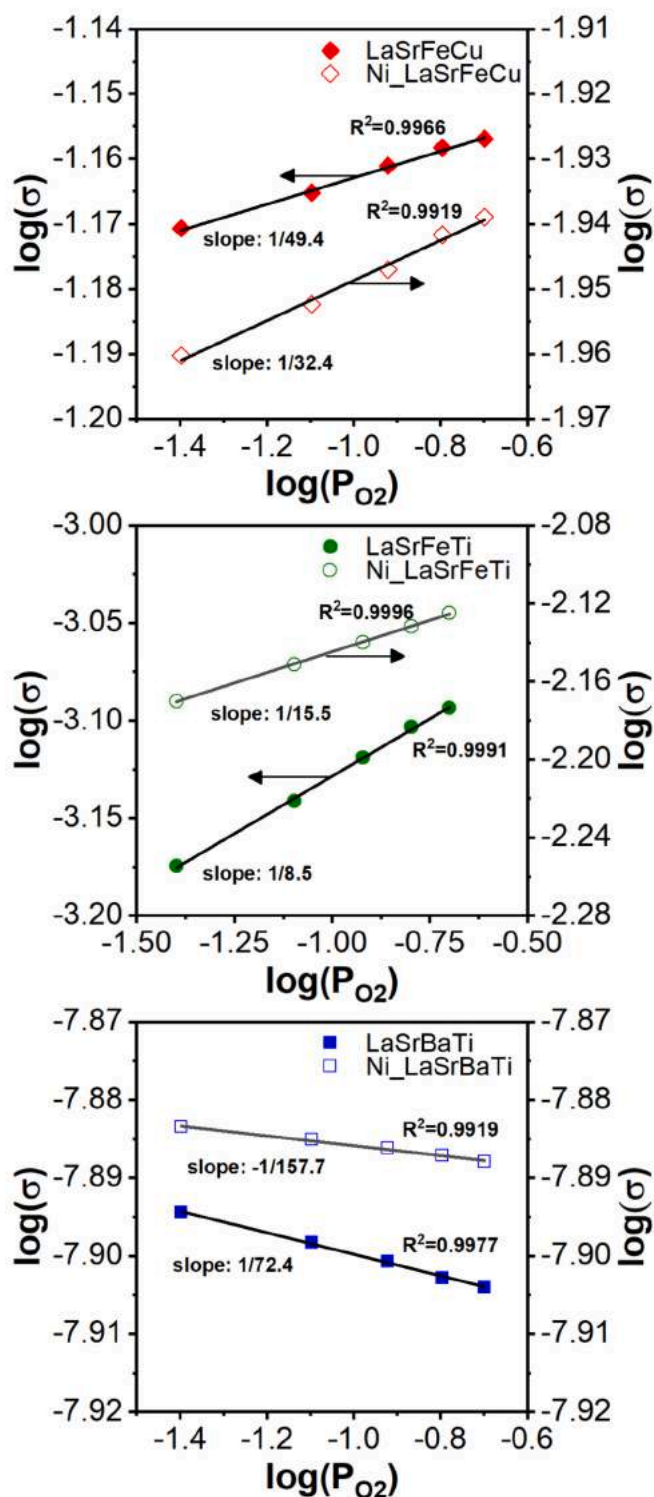

Fig. 8. Variation of σ as a function of the oxygen pressure for the Ni-free and Ni-bearing perovskite samples at 500 °C in log–log plots (P_{O2} in atm; σ in $ohm^{-1}\ cm^{-1}$).

of Ni on the LaSrFeCu perovskite leads to a decrease in the concentration of the positive holes, suggesting either an electron transfer from the metallic Ni particles to the *p*-type semiconducting support, or an increase in the concentration of oxygen vacancies compared to the Ni-free perovskite. Contrarily, the deposition of Ni on the LaSrFeTi perovskite leads to an increase in the concentration of the positive holes, suggesting

either an inverse electron transfer, *i.e.*, from the *p*-type semiconducting support to the metallic Ni particles, or a decrease in the concentration of oxygen vacancies compared to the Ni-free perovskite. It is worth noting that the addition of Ni to LaSrFeCu perovskite results in an increase of the slope of the $\log(\sigma)$ – $\log(P_{O2})$ plot compared to the Ni-free perovskite, which suggests an increased ability of the Ni_LaSrFeCu system to exchange oxygen with the gas phase. On the other hand, a decrease of the slope of the $\log(\sigma)$ – $\log(P_{O2})$ plot is observed for Ni_LaSrFeTi and, hence, a decreased ability of this system to exchange oxygen with the gas phase compared to the Ni-free LaSrFeTi perovskite.
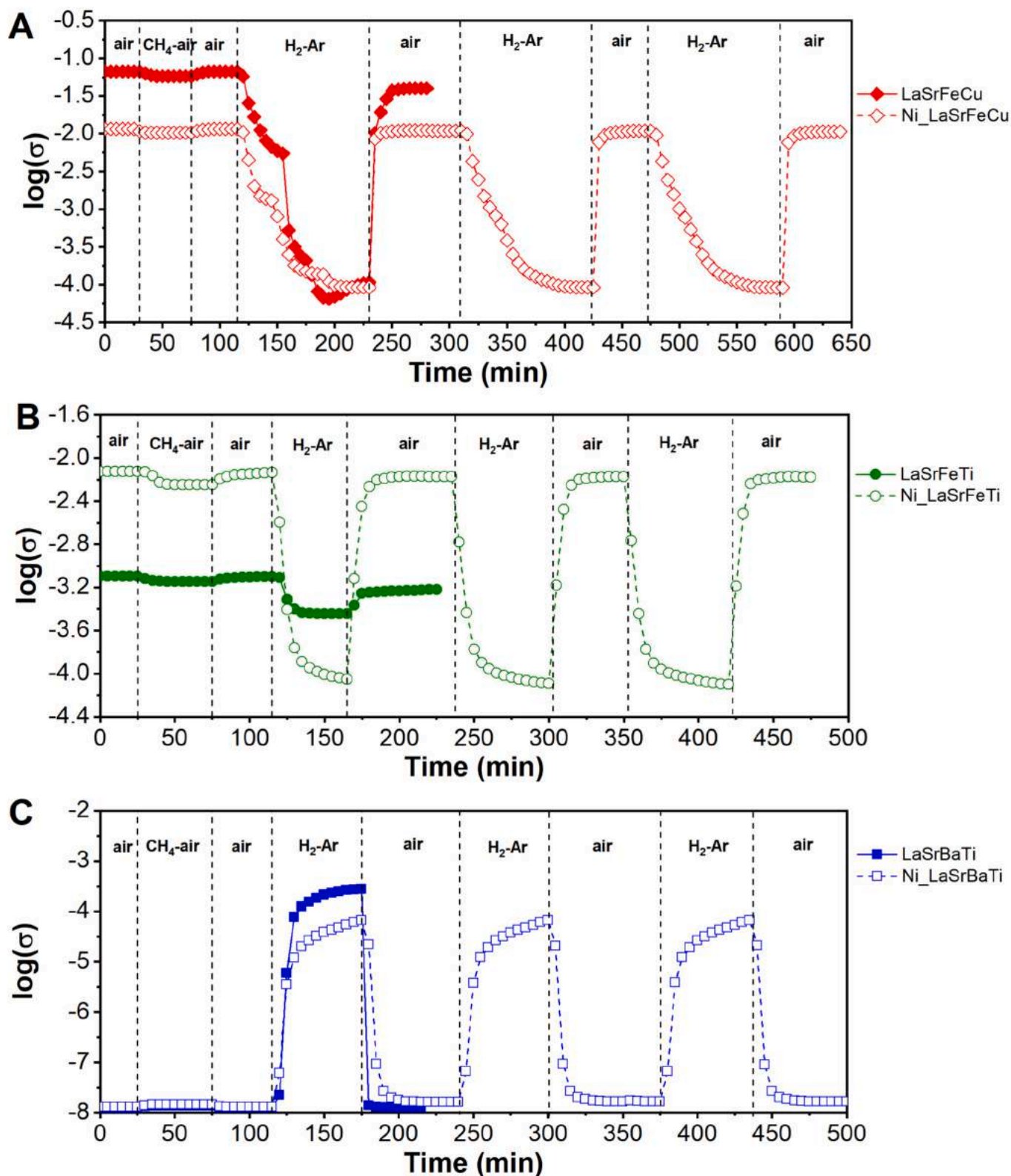

Fig. 9. Variation of the electrical conductivity of the Ni-free and Ni-bearing perovskites A) LaSrFeCu, B) LaSrFeTi and C) LaSrBaTi during sequential exposures to different gas streams at 500 °C (σ in ohm^{-1} cm^{-1}). The dashed vertical lines separate the different gas sequences.

The *n*-type behavior observed for LaSrBaTi perovskite at 500 °C, which shows a log(σ) – log(P$_{O2}$) plot with negative slope, *i.e.*, $\partial\sigma/\partial P_{O2} < 0$, can be explained taking into consideration the temperature-independent behavior of its electrical conductivity observed in the temperature range from *ca.* 290 to 440 °C (Fig. 7). Thus, most probably, at temperatures lower than 290 °C, the LaSrBaTi perovskite is also a *p*-type semiconducting oxide with the charge carriers (positive holes) associated to the substitutional defects of Ti(IV) sitting on Ti(III) lattice points (the B sites in the ABO$_3$ perovskite structure), *i.e.*, $Ti^{\bullet}_{Ti}$. The charge compensation is ensured by the cationic vacancies, V'''_{La}, and the substitutional defects of Sr(II) and Ba(II) sitting on La(III) lattice points (the A sites in the ABO$_3$ perovskite structure), *i.e.*, Sr'_{La} and Ba'_{La}, respectively. At low temperatures, these negatively charged defects associated to energy states in the band gap act as hole traps. With increasing temperature, the holes are liberated from traps, which corresponds to the ionization of these defects resulting in an increase of the density of charge carriers (Eqs. (4, 5 and 6)):

$$V^x_{La} \rightarrow V'''_{La} + 3h^{\bullet} \tag{4}$$

$$Sr^x_{La} \rightarrow Sr'_{La} + h^{\bullet} \tag{5}$$

$$Ba^x_{La} \rightarrow Ba'_{La} + h^{\bullet} \tag{6}$$

and, hence, the *p*-type conductivity of the semiconducting oxide increases. In the temperature range from 290 to 440 °C, the solid simultaneously starts losing lattice oxygen with formation of oxygen vacancies, $V^{\bullet\bullet}_O$, and generation of electrons, e', according to the Eq. (7):

$$O^x_O \rightarrow 1/2 O_2 + V^{\bullet\bullet}_O + 2e' \tag{7}$$

which neutralize the positive holes resulted by the ionization of the defects, explaining the apparent temperature-independent behavior observed [55]. Then, at temperatures higher than 440 °C, the density of conduction electrons becomes higher than that of positive holes and, hence, the *n*-type behavior becomes dominant, as suggested by the variation of σ as a function of the oxygen partial pressure at 500 °C (Fig. 8). Interestingly, the deposition of Ni on the LaSrBaTi perovskite slightly increases the *n*-type conductivity of the solid, suggesting an electron transfer from the metallic Ni particles to the LaSrBaTi perovskite support. At the same time, the slope of the log(σ) – log(P$_{O2}$) plot becomes two times lower (Fig. 8), suggesting that the addition of Ni negatively affects the ability of the material to exchange oxygen with the gas phase according to the Eq. (7).

3.3.3. Study of the redox behavior of the materials by in situ electrical conductivity measurements

The redox behavior of both Ni-free and Ni-bearing perovskite-based mixed oxides was studied by measuring the variation of their electrical conductivity at a temperature close to the catalytic reaction temperature, *i.e.*, 500 °C, under different successive oxidizing and reducing gas streams, *i.e.*, air – CH$_4$/air mixture – air – H$_2$/Ar mixture – air. The variations obtained are shown in Fig. 9. It can be observed that the electrical conductivity of all the *p*-type materials decreased under the CH$_4$-air mixture compared to that under air, indicating the reduction of the oxide under the CH$_4$-air flow, which behaves as a reducing gas mixture. This confirms the *p*-type semiconducting behavior of both Ni-free and Ni-bearing LaSrFeCu and LaSrFeTi perovskites, according to the *p*-type criterion $\partial\sigma/\partial P_{reducing\ gas} < 0$. However, the amplitude of the effect, which is a measure of the extent of reduction of the oxides under the CH$_4$-air mixture, is small in all cases, suggesting that the reduction is rather limited to the surface and subsurface regions of the solids.

Under a new air stream, the electrical conductivity increased to the initial value for all the *p*-type materials, accounting for their complete reoxidation. Notably, according to the *p*-type criterion $\partial\sigma/\partial P_{O2} > 0$, this behavior confirms that all samples remained of *p*-type after reduction

under the CH$_4$-air mixture. Under the H$_2$—Ar mixture, the electrical conductivity has a peculiar behavior for each of the *p*-type materials studied.

Thus, when the H$_2$—Ar mixture flows over the Ni-free LaSrFeCu perovskite leads to a stepwise decrease of the electrical conductivity, followed by a final slight increase before reaching the steady state. Indeed, the introduction of the H$_2$—Ar flow over this sample leads, as expected, to a decrease of the electrical conductivity, which seems to tend to a plateau, but at 155th minute it suddenly decreases by more than one order of magnitude followed by a new quick decrease at 175th minute, then it passes through a minimum at 195th minute and, finally, slightly increases to reach the plateau corresponding to the steady state. Based on the X-ray diffraction analysis, which shows that La$_{0.8}$Sr$_{0.2}$Fe$_{0.95}$Cu$_{0.05}$O$_3$ perovskite is the main crystalline phase identified in LaSrFeCu mixed oxide, together with tiny amounts of SrCO$_3$ and CuO side-phases, obviously the conductivity of the perovskite phase prevails. Thus, the first and the second decreasing steps of the electrical conductivity account for the stepwise reduction of the B-type cations from the perovskite structure, *i.e.*, Fe(IV) → Fe(III) and Cu(II) → Cu(I) in the first step, followed by Fe(III) → Fe(II) and Cu(I) → Cu^0 in the second step. The last decrease of the electrical conductivity, followed by a slight increase before reaching the steady state is quite similar to the behavior of CuO under a reducing gaseous atmosphere [56], and, hence, it is attributed to the reduction of tiny CuO particles identified in the LaSrFeCu sample: Cu(II) → Cu(I) followed by Cu(I) → Cu^0 accounting for the decreasing and increasing steps of the electrical conductivity, respectively. This suggests that the CuO crystallites are not distributed on the surface of the perovskite phase, but they are rather buried into the perovskite matrix, forming a kind of core-shell particles with a tiny CuO core and a thinner perovskite shell. This is in line with the low intensity of the Cu *2p* XPS spectra peaks observed. Finally, when a new air sequence is introduced over the reduced Ni-free LaSrFeCu sample, the electrical conductivity increases and reaches a new steady state, which is different from the initial steady state under air. This suggests that LaSrFeCu sample is not completely reoxidized after being reduced under the H$_2$—Ar mixture. Notably, the electrical conductivity of the sample under the H$_2$—Ar flow varies within *ca.* four orders of magnitude accounting for a profound (bulk) reduction of the mixed oxide.

The behavior of the Ni-bearing LaSrFeCu perovskite under the H$_2$—Ar mixture is similar to that of the Ni-free sample, the electrical conductivity reaching practically the same steady state corresponding to the complete reduction of both solids. However, the last decreasing step of the electrical conductivity of the Ni_LaSrFeCu sample under this reduction mixture leads directly to the steady state, without passing through a minimum followed by an increase of the electrical conductivity, as observed for the Ni-free LaSrFeCu sample. This suggests that in the presence of Ni, the reduction of the tiny CuO particles from the perovskite matrix takes place in a single step: Cu(II) → Cu^0. This is obviously due to the participation in the reduction event of the spilled over atomic hydrogen formed by the dissociation of molecular H$_2$ on the metallic Ni particles [57]. Interestingly, when the final air sequence is introduced over the reduced Ni_LaSrFeCu sample, its electrical conductivity increased to the initial value suggesting its complete reoxidation.

The electrical conductivity of the LaSrFeTi sample, which consists of La$_{0.5}$Sr$_{0.5}$Fe$_{0.5}$Ti$_{0.5}$O$_3$ perovskite phase with tiny amounts of SrCO$_3$ side-phase, decreases under the H$_2$—Ar mixture within less than one order of magnitude, suggesting no deep reduction of this material. However, the reduction is deeper than under the CH$_4$-air mixture. Then, under a new air stream the electrical conductivity increases and reaches a new steady state, which is different from the initial steady state under air. This suggests that LaSrFeTi sample is only partially reoxidized after being reduced under the H$_2$—Ar mixture. On the other hand, the electrical conductivity of the Ni_LaSrFeTi sample strongly decreases under the H$_2$—Ar mixture accounting for its profound reduction obviously due to the involvement of the of the spilled over atomic hydrogen formed by

the dissociation of dihydrogen on the metallic Ni particles present in this material. Again, the reoxidation of the Ni-bearing LaSrFeTi material is almost complete under the final air stream as its electrical conductivity increased to a value close to the initial value. It seems that the reoxidation of the *p*-type perovskites reduced under H_2, which is only partial in the absence of Ni, is favored by the presence of metallic nickel particles, becoming, thus, complete.

The data in Fig. 9 show that the electrical conductivity of the *n*-type materials under air is significantly lower compared to their *p*-type counterparts. Under the CH_4-air mixture, the electrical conductivity of both Ni-free and Ni-bearing *n*-type LaSrBaTi perovskites slightly increased compared to that under air. This corresponds to the reduction of the oxide in the presence of the CH_4-air mixture, which behaves as a reducing gas stream. According to the *n*-type criterion $\partial\sigma/\partial P_{reducing\ gas} > 0$, this confirms their *n*-type semiconducting behavior. Notably, the amplitude of the effect is small accounting for a low degree of reduction of the solids under the CH_4-air mixture, which is most likely limited to the surface region. When a new air stream was introduced over the *n*-type samples, their electrical conductivity regained its initial value (Fig. 9), suggesting that they are completely reoxidized. According to the *n*-type criterion $\partial\sigma/\partial P_{O2} < 0$, this behavior confirms that the samples remained of *n*-type after reduction under the CH_4-air mixture.

The introduction of a H_2—Ar mixture over the *n*-type solids after the second air sequence leads to a strong increase of their electrical conductivities of several orders of magnitude (Fig. 9), that of the Ni-free perovskite being higher than that of the Ni-bearing material at steady state. This suggests that, compared to the reduction under the CH_4-air mixture, which is limited to the surface and subsurface regions, under the H_2—Ar mixture both *n*-type solids are profoundly reduced. However, unexpectedly, the Ni-bearing LaSrBaTi perovskite is, at steady state, less reduced than the Ni-free mixed oxide. Under the final air stream, the electrical conductivities of both solids immediately decrease reaching plateaus close to the initial steady state under air. This clearly suggests that the re-oxidation of both Ni-free and Ni-bearing LaSrBaTi perovskites reduced under H_2 is completely reversible. However, a close inspection of the curves corresponding to the reoxidation of the reduced solids shows different reoxidation rates. Indeed, the reoxidation rate, $d\sigma/dt$, of the Ni-free LaSrBaTi perovskite is higher than that of Ni-LaSrBaTi. These results point to an unfavorable effect of metallic Ni particles on the redox properties of the *n*-type LaSrBaTi perovskite. This is in line with the observed negative effect of Ni on the ability of the LaSrBaTi material to exchange oxygen with the gas phase (section 3.3.2).

Since the Ni-bearing samples are used as catalysts, their behavior was further studied during two supplementary reduction-reoxidation cycles under H_2—Ar mixture and under air, respectively. As it can be observed in Fig. 9, all the systems return to their original reduced or oxidized states after each new cycle. No noticeable changes could be observed in the behavior of Ni_LaSrFeTi and Ni_LaSrBaTi samples during the two supplementary reduction-reoxidation cycles, whereas the stepwise reduction of the cations in the Ni_LaSrFeCu sample during the new reduction sequences became less marked, suggesting an improved electron transfer in the solid after a few reduction-reoxidation cycles.

To summarize, the *in situ* electrical conductivity measurements during sequential periods under reducing (CH_4-air and H_2—Ar mixtures) and oxidizing (air) gas streams clearly demonstrate that all Ni-free and Ni-bearing perovskite-based materials are in a slightly reduced state under the CH_4-air mixture and profoundly reduced under the H_2—Ar mixture. LaSrBaTi perovskite is of *n*-type, while LaSrFeCu and LaSrFeTi perovskites are of *p*-type, the nature of their conductivity remaining the same after the deposition of metallic Ni particles on their surface. The *n*-type materials are completely reoxidized under air after the reduction steps, in particular after the H_2—Ar sequence. However, the reduction is deeper and the reoxidation process is faster for the Ni-free compared to Ni-bearing LaSrBaTi perovskite. On the other hand, the Ni-free *p*-type perovskites reduced under H_2 are only partially reoxidized compared to

their Ni-bearing counterparts, which return to their original reduced or oxidized states after several reduction-oxidation cycles. Obviously, the nickel deposition strongly influences the semiconductive and redox properties of all the perovskites studied.

3.4. Catalytic tests

All the metal catalysts tested towards the catalytic activity in the autothermal reforming of CH_4 and model biogas did not show relevant results, as reported in Fig. S5 and S6 (supporting information section). According to other studies [26,58–60], the reactivity of CH_4 and biogas is low in the ATR condition at temperatures lower than 800 °C. Conversely, the autothermal reforming of EtOH showed a significant production of syngas, providing interesting results (Fig. 10). All the metal catalysts showed almost a full conversion of EtOH at both reaction
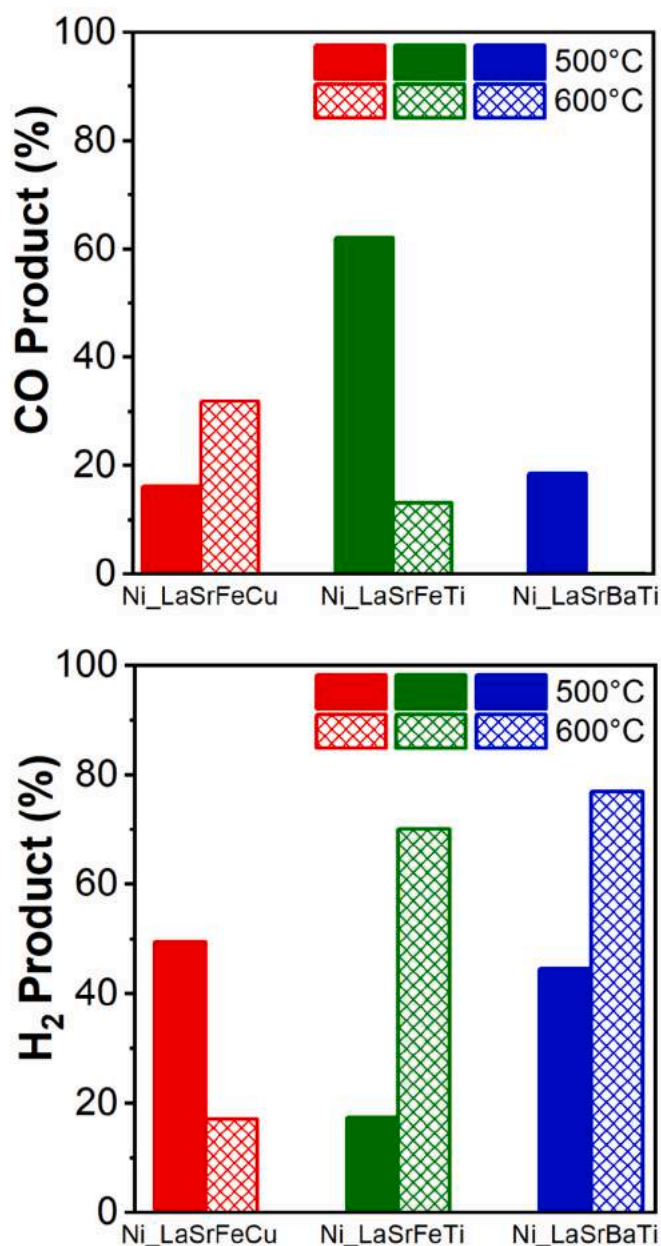

Fig. 10. H_2 and CO production by ATR of Ethanol on Ni-based perovskite catalysts.

temperatures considered, 500 °C and 600 °C, as shown in Fig. 10.

The most interesting results came from Ni_LaSrFeTi and Ni_LaSrBaTi. In particular, at 600 °C, Ni_LaSrFeTi has high selectivity to syngas production, which is up to 83 vol% in terms of CO + H$_2$ obtained. However, if the distribution of the reaction product in the outlet stream is analyzed, the Ni_LaSrBaTi exhibited the highest H$_2$/CO ratio compared to the other samples, as reported in Table 5. Depending on the temperature conditions, the results were probably correlated with the different compositional and structural formulations of perovskites.

The good performances of the synthesized Ni-based catalysts are also due to the porous structure of the perovskite support, which provides higher surface area and, thus, higher dispersion of the active phase. In the literature, supported catalysts are commonly investigated for ATR of ethanol [61–64]. As an example, Peela and Kunzru [62] used different catalysts, such as 1%Rh/Al$_2$O$_3$, 1%Rh–20%Ce/Al$_2$O$_3$ and 2%Rh–20% Ce/Al$_2$O$_3$, the last sample evidencing the highest product selectivity and activity. CeO$_2$ promoted Rh performances thanks to its high oxygen storage capacity and redox properties, but still the presence of alumina was assumed necessary. Han et al. [63] supported Rh over mixed Ce—La systems, in which La allowed to improve the surface area of CeO$_2$; this positive effect resulted in total conversion of ethanol at 300 °C when CeO$_2$ was doped with 30 mol% La. Furtado et al. [64] evidenced that the support plays a crucial role on the metallic dispersion of Ni-Cu-based catalysts. In fact, the highest ethanol conversion was noticed for Ni–Cu/α-Al$_2$O$_3$, while the highest H$_2$ selectivity was observed for Ni–Cu/Ce$_{0.6}$Zr$_{0.4}$O$_2$. Also, in this case the good dispersion of the active phase on the Ce—Zr oxide support was related to increased presence of active oxygen, which prevented the formation of coke. In all these studies [62–64], the dispersion of the active phase on a support material with higher surface area was crucial for increasing the number of possible active sites, thus improving the final performances.

Since the evaluation of the stability of a catalyst is crucial for its possible applications [65], the spent materials obtained after ATR tests at different temperatures were characterized by XRD, not only to identify possible structural modifications but also to investigate the formation of carbon species. In addition, coupled TGA-DTGA and SEM-EDX analyses were also used to estimate the amount of deposited coke. X-ray diffraction analysis evidenced that the pristine perovskite structures of the Ni_LaSrFeCu and Ni_LaSrFeTi samples were not stable under the reaction conditions (Fig. 11). This was not the case for Ni_LaSrBaTi, which showed good stability at both reaction temperatures used. Thus, despite the syngas production of Ni_LaSrBaTi (78%) is slightly lower than that of Ni_LaSrFeTi (83%), the former sample may be more suitable for the reaction conditions used, due to its good stability at intermediate temperatures. Different carbon content was detected for the different catalytic systems. In particular, a higher quantity of carbon was detected in the spent Ni_LaSrFeCu and Ni_LaSrFeTi, as evident from the XRD patterns in Fig. 11, in which the line at 26° indicates the formation of coke.

This was also confirmed by both TGA and SEM-EDX analyses, as reported for example in the case of the Ni_LaSrFeCu catalyst after ATR reaction at 600 °C (Fig. 12).

Indeed, the TGA-DTGA profile of the spent catalyst exhibited an exothermic peak at about 600 °C, corresponding to the combustion of the deposited carbon. The overall carbon content over the analyzed spent catalysts is reported in Fig. 13.

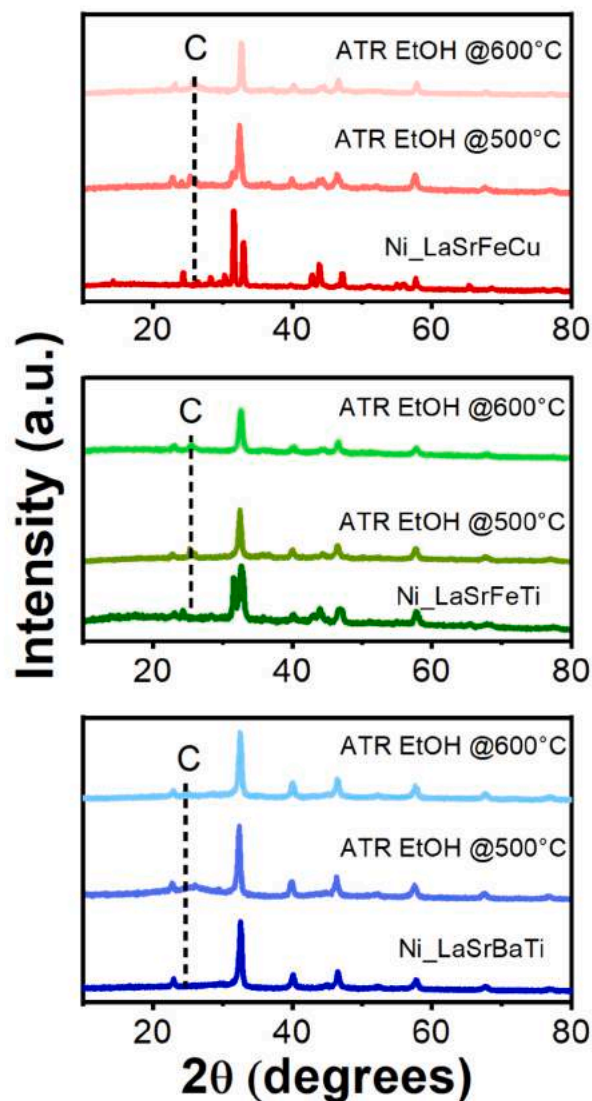In line with XRD analysis, large amounts of carbon were revealed in

Fig. 11. XRD profiles of spent catalyst after ATR of Ethanol Reaction.
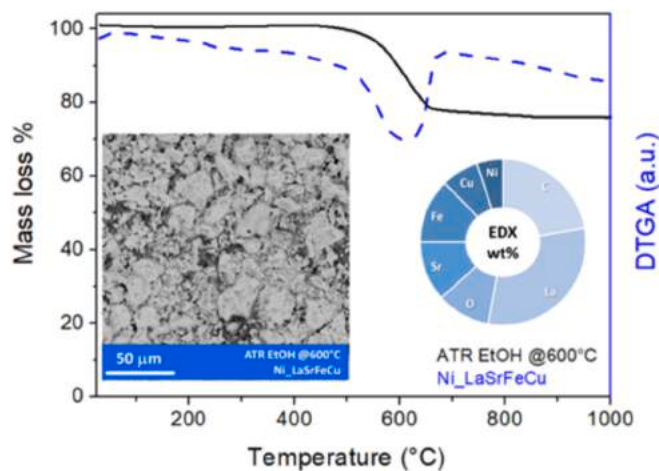
Fig. 12. SEM-EDX and TG-DTA analysis of Ni_LaSrFeCu after ATR of Ethanol at 600 °C.

Table 5
H$_2$/CO molar ratio of the outlet stream under EtOH ATR condition.

Sample	H$_2$/CO @500 °C	H$_2$/CO @600 °C
Ni_LaSrFeCu	3.1	0.5
Ni_LaSrFeTi	0.3	5.4
Ni_LaSrBaTi	2.4	770*

* CO trace in the gas outlet stream.
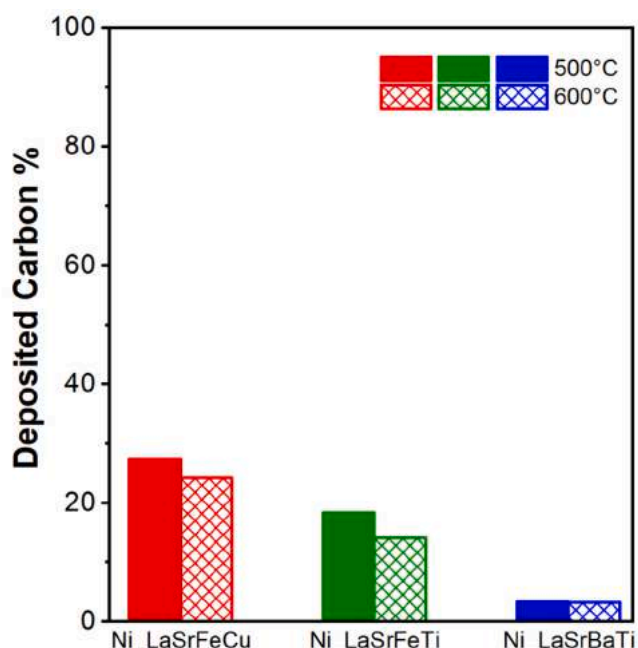
Fig. 13. Amount of carbon after ATR of Ethanol on Nickel based perovskite catalysts.

both Ni_LaSrFeCu and Ni_LaSrFeTi, whereas the carbon quantity detected over the Ni_LaSrBaTi sample was scarce, for both tested temperatures. Interestingly, irrespectively of the nature of the electrical conductivity of the catalyst, the deposited carbon content increases with increasing the σ_0 value, which depends on the concentration of the charge carriers in the semiconducting material. This could suggest that the charge carriers, either electrons or positive holes, are involved in the surface bonding of the intermediates responsible for the coke formation.

The Ni_LaSrBaTi catalyst was also submitted to a stress stability test, cooling the sample down at room temperature and heating it up to the reaction temperature, where it was kept on stream for 10 h. After repeating five times this cycle, the catalyst exhibited a loss of catalytic performance of 10% and an increment of deposited carbon of 30%. Nevertheless, this carbon does not significantly deactivate the catalyst, probably because the decomposition of ethanol leads to the formation of ordered coke that does not sensibly affect the performance of the material [60,66].

4. Conclusions

Among the three synthesized perovskites, the physico-chemical characterization revealed that the most interesting materials were LaSrFeTi and LaSrBaTi, which exhibited relatively high surface area and pore volume. In particular, LaSrBaTi exhibited a very stable crystal structure, which was fully preserved after impregnation of Ni and reducing treatment for catalyst activation. In contrast, the other two samples can be more easily reduced, and this results in a less stable structure and in a lower Ni dispersion.

The electrical conductivity measurements showed that LaSrBaTi was of *n*-type, while LaSrFeCu and LaSrFeTi were of *p*-type. Their redox properties were strongly influenced by the deposition of metallic Ni particles on their surface, but the nature of their conductivity remained the same. The *n*-type materials were completely reoxidized under air after reduction, but the process was faster and deeper for the Ni-free LaSrBaTi sample compared to the Ni-bearing one. On the other hand, the Ni-free *p*-type perovskites were only partially reoxidized compared to their Ni-bearing counterparts. The electrical conductivity behavior under the different reducing gas streams suggests that the Ni-bearing

perovskite catalysts are partially reduced under the ATR reaction mixtures.

The catalytic performance of the Ni-based perovskite catalysts was evaluated for different fuels: very low conversions were observed for the ATR of model biogas and CH_4, due to the low reaction temperature used, whereas ATR of ethanol led to significant syngas production. The EtOH ATR tests showed that the Ni_LaSrFeTi sample exhibited high reactivity for syngas production at 600 °C with a high H_2/CO ratio. However, it also showed a moderate deposit of carbon over time, which decreased its performance. The charge carriers, either electrons or positive holes, seem to be involved in the surface bonding of the intermediates responsible for the coke formation. On the other hand, the Ni_LaSrBaTi sample exhibited complete conversion, a very high H_2 selectivity (almost 100%), and a low carbon deposition. Moreover, this perovskite showed superior stability compared to the other two samples: indeed, its crystalline structure remained stable not only after Ni impregnation and activation but also after the catalytic tests, as confirmed by XRD. Hence, Ni_LaSrBaTi can be considered a promising catalyst for the production of hydrogen-rich syngas through ethanol ATR in IT-SOFC.

CRediT authorship contribution statement

Melodj Dosa: Investigation, Formal analysis, Data curation, Writing – original draft. **Enrico Sartoretti:** Data curation, Writing – review & editing. **Alessandro Monteverde:** Writing – review & editing. **Samir Bensaid:** Supervision. **Ionel Popescu:** Investigation, Validation, Data curation. **Ioan-Cezar Marcu:** Methodology, Data curation, Writing - review & editing. **Patrizia Frontera:** Writing - review & editing. **Angela Malara:** Formal analysis, Data curation. **Anastasia Macario:** Formal analysis, Data curation. **Marco Piumetti:** Methodology, Conceptualization, Supervision.

Declaration of competing interest

The authors declare that they have no known competing financial interests or personal relationships that could have appeared to influence the work reported in this paper.

Data availability

Data will be made available on request.

Appendix A. Supplementary data

Supplementary data to this article can be found online at https://doi.org/10.1016/j.apcato.2024.206959.

References

[1] R.M. Ormerod, Solid oxide fuel cells, Chem. Soc. Rev. 32 (2003) 17–28, https://doi.org/10.1039/b105764m.

[2] P. Boldrin, N.P. Brandon, Progress and outlook for solid oxide fuel cells for transportation applications, Nat. Catal. 2 (2019) 571–577, https://doi.org/10.1038/s41929-019-0310-y.

[3] A.M. Abdalla, S. Hossain, A.T. Azad, P.M.I. Petra, F. Begum, S.G. Eriksson, A.K. Azad, Nanomaterials for solid oxide fuel cells: a review, Renew. Sust. Energ. Rev. 82 (2018) 353–368, https://doi.org/10.1016/j.rser.2017.09.046.

[4] B. Song, E. Ruiz-Trejo, A. Bertei, N.P. Brandon, Quantification of the degradation of Ni-YSZ anodes upon redox cycling, J. Power Sources 374 (2018) 61–68, https://doi.org/10.1016/j.jpowsour.2017.11.024.

[5] M.S. Khan, S.B. Lee, R.H. Song, J.W. Lee, T.H. Lim, S.J. Park, Fundamental mechanisms involved in the degradation of nickel–yttria stabilized zirconia (Ni–YSZ) anode during solid oxide fuel cells operation: a review, Ceram. Int. 42 (2016) 35–48, https://doi.org/10.1016/j.ceramint.2015.09.006.

[6] V. Subotić, C. Schluckner, B. Stoeckl, M. Preininger, V. Lawlor, S. Pofahl, H. Schroettner, C. Hochenauer, Towards practicable methods for carbon removal from Ni-YSZ anodes and restoring the performance of commercial-sized ASC-SOFCs after carbon deposition induced degradation, Energy Convers. Manag. 178 (2018) 343–354, https://doi.org/10.1016/j.enconman.2018.10.022.

[7] J. Hanna, W.Y. Lee, Y. Shi, A.F. Ghoniem, Fundamentals of electro- and thermochemistry in the anode of solid-oxide fuel cells with hydrocarbon and syngas fuels, Prog. Energy Combust. Sci. 40 (2014) 74–111, https://doi.org/10.1016/j.pecs.2013.10.001.

[8] Z. Lyu, W. Shi, M. Han, Electrochemical characteristics and carbon tolerance of solid oxide fuel cells with direct internal dry reforming of methane, Appl. Energy 228 (2018) 556–567, https://doi.org/10.1016/j.apenergy.2018.06.114.

[9] A. Brouzgou, A. Demin, P. Tsiakaras, Advances in Medium And High Temperature Solid Oxide Fuel Cell Technology, Springer International Publishing, Cham, 2017, https://doi.org/10.1007/978-3-319-46146-5.

[10] J. Molenda, K. Świerczek, W. Zajac, Functional materials for the IT-SOFC, J. Power Sources 173 (2007) 657–670, https://doi.org/10.1016/J.JPOWSOUR.2007.05.085.

[11] A. Sinha, D.N. Miller, J.T.S. Irvine, Development of novel anode material for intermediate temperature SOFC (IT-SOFC), J. Mater Chem. A Mater. 4 (2016) 11117–11123, https://doi.org/10.1039/C6TA03404G.

[12] I.Z. Rahman, M.A. Raza, M.A. Rahman, Perovskite based anode materials for solid oxide fuel cell application: a review, in: Adv Mat Res, Trans Tech Publications Ltd, 2012, pp. 497–502, https://doi.org/10.4028/www.scientific.net/AMR.445.497.

[13] L. Shu, J. Sunarso, S.S. Hashim, J. Mao, W. Zhou, F. Liang, Advanced perovskite anodes for solid oxide fuel cells: a review, Int. J. Hydrog. Energy 44 (2019) 31275–31304, https://doi.org/10.1016/j.ijhydene.2019.09.220.

[14] A. Yaqub, C. Savaniu, N.K. Janjua, J.T.S. Irvine, Preparation via a solution method of La0.2Sr0.25Ca0.45TiO3 and its characterization for anode supported solid oxide fuel cells, J. Mater. Chem. A Mater. 1 (2013) 14189–14197, https://doi.org/10.1039/c3ta12860a.

[15] K.Y. Lai, A. Manthiram, Self-regenerating co-Fe nanoparticles on perovskite oxides as a hydrocarbon fuel oxidation catalyst in solid oxide fuel cells, Chem. Mater. 30 (2018) 2515–2525, https://doi.org/10.1021/acs.chemmater.7b04569.

[16] Y. Sun, J. Li, Y. Zeng, B.S. Amirkhiz, M. Wang, Y. Behnamian, J. Luo, A-site deficient perovskite: the parent for in situ exsolution of highly active, regenerable nano-particles as SOFC anodes, J Mater. Chem. A Mater. 3 (2015) 11048–11056, https://doi.org/10.1039/c5ta01733e.

[17] M.C. Verbraeken, T. Ramos, K. Agersted, Q. Ma, C.D. Savaniu, B.R. Sudireddy, J.T. S. Irvine, P. Holtappels, F. Tietz, Modified strontium titanates: from defect chemistry to SOFC anodes, RSC Adv. 5 (2015) 1168–1180, https://doi.org/10.1039/c4ra09751c.

[18] M.A. Peña, J.L.G. Fierro, Chemical structures and performance of perovskite oxides, Chem. Rev. 101 (2001) 1981–2017, https://doi.org/10.1021/cr980129f.

[19] M. Ghelamallah, S. Kacimi, R.I. Fertout, Incorporation of barium in titanium oxide and lanthanum oxide, Mater. Lett. 59 (2005) 714–718, https://doi.org/10.1016/j.matlet.2004.06.072.

[20] P.R.N. Silva, A.B. Soares, Lanthanum based high surface area perovskite-type oxide and application in CO and propane combustion, Ecletica Quim. 34 (2009) 31–38, https://doi.org/10.26850/1678-4618EQJ.V34.1.2009.P31-38.

[21] S. Specchia, A. Civera, G. Saracco, In situ combustion synthesis of perovskite catalysts for efficient and clean methane premixed metal burners, Chem. Eng. Sci. 59 (2004) 5091–5098, https://doi.org/10.1016/J.CES.2004.08.028.

[22] E. García-López, G. Marcì, F. Puleo, V. La Parola, L.F. Liotta, La1-xSrxCo1-yFeyO3-δ perovskites: preparation, characterization and solar photocatalytic activity, Appl. Catal. B 178 (2015) 218–225, https://doi.org/10.1016/j.apcatb.2014.09.014.

[23] Y.H. Huang, R.I. Dass, Z.L. King, J.B. Goodenough, Double perovskites as anode materials for solid-oxide fuel cells, Science 312 (2006) (1979) 254–257, https://doi.org/10.1126/science.1125877.

[24] B. Kayaalp, S. Lee, K. Klauke, J. Seo, L. Nodari, A. Kornowski, W.C. Jung, S. Mascotto, Template-free mesoporous La0.3Sr0.7FexTi1-xO3±Δ with superior oxidation catalysis performance, Appl. Catal. B 245 (2019) 536–545, https://doi.org/10.1016/j.apcatb.2018.12.077.

[25] M. Piumetti, S. Bensaid, T. Andana, N. Russo, R. Pirone, D. Fino, Cerium-copper oxides prepared by solution combustion synthesis for total oxidation reactions: from powder catalysts to structured reactors, Appl. Catal. B 205 (2017) 455–468, https://doi.org/10.1016/j.apcatb.2016.12.054.

[26] M. Lo Faro, R.M. Reis, G.G.A. Saglietti, V.L. Oliveira, S.C. Zignani, S. Trocino, S. Maisano, E.A. Ticianelli, N. Hodnik, F. Ruiz-Zepeda, A.S. Aricò, Solid oxide fuel cells fed with dry ethanol: the effect of a perovskite protective anodic layer containing dispersed Ni-alloy @ FeOx core-shell nanoparticles, Appl. Catal. B 220 (2018) 98–110, https://doi.org/10.1016/j.apcatb.2017.08.010.

[27] P. Frontera, A. Malara, V. Modafferi, V. Antonucci, P. Antonucci, A. Macario, Catalytic activity of Ni-co supported metals in carbon dioxides methanation, Can. J. Chem. Eng. (2020), https://doi.org/10.1002/cjce.23780.

[28] J.-M. Herrmann, Applications of Electrical Conductivity Measurements in Heterogeneous Catalysis, 1994, pp. 559–584, https://doi.org/10.1007/978-1-4757-9589-9_20.

[29] P. Frontera, A. Macario, A. Malara, S. Santangelo, C. Triolo, F. Crea, P. Antonucci, Trimetallic ni-based catalysts over gadolinia-doped ceria for green fuel production, Catalysts 8 (2018), https://doi.org/10.3390/catal8100435.

[30] P. Priya, N.R. Aluru, Accelerated design and discovery of perovskites with high conductivity for energy applications through machine learning, Npj Comput. Mater. 7:1 (7) (2021) 1–12, https://doi.org/10.1038/s41524-021-00551-3.

[31] M. Thommes, K. Kaneko, A.V. Neimark, J.P. Olivier, F. Rodriguez-Reinoso, J. Rouquerol, K.S.W. Sing, Physisorption of gases, with special reference to the evaluation of surface area and pore size distribution (IUPAC technical report), Pure Appl. Chem. 87 (2015) 1051–1069, https://doi.org/10.1515/pac-2014-1117.

[32] M.J. Marin Figueredo, T. Andana, S. Bensaid, M. Dosa, D. Fino, N. Russo, M. Piumetti, Cerium–copper–manganese oxides synthesized via solution combustion synthesis (SCS) for Total oxidation of VOCs, Catal. Lett. 150 (2020) 1821–1840, https://doi.org/10.1007/s10562-019-03094-x.

[33] M. Piumetti, T. Andana, S. Bensaid, N. Russo, D. Fino, R. Pirone, Study on the CO oxidation over ceria-based Nanocatalysts, Nanoscale Res. Lett. 11 (2016) 165, https://doi.org/10.1186/s11671-016-1375-z.

[34] K. Ji, H. Dai, J. Deng, L. Zhang, F. Wang, H. Jiang, C.T. Au, Three-dimensionally ordered macroporous SrFeO3-δ with high surface area: active catalysts for the complete oxidation of toluene, Appl. Catal. A Gen. 425–426 (2012) 153–160, https://doi.org/10.1016/j.apcata.2012.03.013.

[35] A. Gervasini, Temperature programmed reduction/oxidation (TPR/TPO) methods, in: Springer Series in Materials Science, Springer Science and Business Media Deutschland GmbH, 2013, pp. 175–195, https://doi.org/10.1007/978-3-642-11954-5_5.

[36] J. Yang, S. Hu, Y. Fang, S. Hoang, L. Li, W. Yang, Z. Liang, J. Wu, J. Hu, W. Xiao, C. Pan, Z. Luo, J. Ding, L. Zhang, Y. Guo, Oxygen vacancy promoted O2 activation over perovskite oxide for low-temperature CO oxidation, ACS Catal. 9 (2019) 9751–9763, https://doi.org/10.1021/ACSCATAL.9B02408/ASSET/IMAGES/LARGE/CS9B02408_0006.JPEG.

[37] M. Dosa, M. Piumetti, S. Bensaid, T. Andana, C. Novara, F. Giorgis, D. Fino, N. Russo, Novel Mn–cu-containing CeO2 Nanopolyhedra for the oxidation of CO and diesel soot: effect of dopants on the nanostructure and catalytic activity, Catal. Lett. 148 (2018) 298–311, https://doi.org/10.1007/s10562-017-2226-y.

[38] T. Andana, M. Piumetti, S. Bensaid, N. Russo, D. Fino, R. Pirone, CO and soot oxidation over Ce-Zr-Pr oxide catalysts, Nanoscale Res. Lett. 11 (2016) 278, https://doi.org/10.1186/s11671-016-1494-6.

[39] M. Konsolakis, S.A.C. Carabineiro, G.E. Marnellos, M.F. Asad, O.S.G.P. Soares, M.F. R. Pereira, J.J.M. Órfão, J.L. Figueiredo, Volatile organic compounds abatement over copper-based catalysts: effect of support, Inorg. Chim. Acta 455 (2017) 473–482, https://doi.org/10.1016/j.ica.2016.07.059.

[40] T. Andana, M. Piumetti, S. Bensaid, N. Russo, D. Fino, R. Pirone, Nanostructured ceria-praseodymia catalysts for diesel soot combustion, Appl. Catal. B 197 (2016) 125–137, https://doi.org/10.1016/j.apcatb.2015.12.030.

[41] L. Soler, A. Casanovas, C. Escudero, V. Pérez-Dieste, E. Aneggi, A. Trovarelli, J. Llorca, Ambient pressure photoemission spectroscopy reveals the mechanism of carbon soot oxidation in ceria-based catalysts, Chem. Cat. Chem. 8 (2016) 2748–2751, https://doi.org/10.1002/cctc.201600615.

[42] R.P. Vasquez, SrCO3 by XPS, Surf. Sci. Spectra. 1 (1992) 112–116, https://doi.org/10.1116/1.1247696.

[43] Y. Xu, X. Zhong, Y. Li, J. Liu, Morphology-controllable self-assembly of strontium carbonate (SrCO3) crystals under the action of different regulators, J. Mater. Sci. Mater. Electron. 30 (2019) 21150–21159, https://doi.org/10.1007/s10854-019-02487-3.

[44] M.F. Sunding, K. Hadidi, S. Diplas, O.M. Løvvik, T.E. Norby, A.E. Gunnæs, XPS characterisation of in situ treated lanthanum oxide and hydroxide using tailored charge referencing and peak fitting procedures, J. Electron Spectrosc. Relat. Phenom. 184 (2011) 399–409, https://doi.org/10.1016/j.elspec.2011.04.002.

[45] L. Liu, W. Li, Z. Xiong, D. Xia, C. Yang, W. Wang, Y. Sun, Synergistic effect of iron and copper oxides on the formation of persistent chlorinated aromatics in iron ore sintering based on in situ XPS analysis, J. Hazard. Mater. 366 (2019) 202–209, https://doi.org/10.1016/j.jhazmat.2018.11.105.

[46] D.D. Hawn, B.M. DeKoven, Deconvolution as a correction for photoelectron inelastic energy losses in the core level XPS spectra of iron oxides, Surf. Interface Anal. 10 (1987) 63–74, https://doi.org/10.1002/sia.740100203.

[47] M. Dosa, M. Piumetti, S. Bensaid, T. Andana, C. Galletti, D. Fino, N. Russo, Photocatalytic abatement of volatile organic compounds by TiO2 nanoparticles doped with either phosphorous or zirconium, Materials 12 (2019), https://doi.org/10.3390/ma12132121.

[48] J.F. Moulder, W.F. Stickle, P.E. Sobol, K.D. Bomben, Handbook of Photoelectron Spectroscopy, Physical Electronics, Inc., Eden Prairie, Minnesota, 1992, https://doi.org/10.1002/sia.740030412.

[49] L. Shen, Z. Du, Y. Zhang, X. Dong, H. Zhao, Medium-entropy perovskites Sr(FeαTiβCoγMnζ)O3-δ as promising cathodes for intermediate temperature solid oxide fuel cell, Appl. Catal. B 295 (2021), https://doi.org/10.1016/j.apcatb.2021.120264.

[50] Z. Sun, Z. Liu, C. Cai, H. Deng, F. Yang, Y. Lu, X. Song, S. An, H. Zhao, High performance oxygen permeation membrane: Sr and Ti co-doped BaFeO3-δ ceramics, Sep. Purif. Technol. 289 (2022) 120742, https://doi.org/10.1016/J.SEPPUR.2022.120742.

[51] Z. Zhang, M. Baerns, X.E. Verykios, Effect of electronic properties of catalysts for the oxidative coupling of methane on their selectivity and activity, Catal. Rev. 36 (1994) 507–556, https://doi.org/10.1080/01614949408009470.

[52] J.B. Goodenough, J.-S. Zhou, in: J.B. Goodenough (Ed.), Localized to Itinerant Electronic Transitions in Perovskite-Related Structures, Springer, Berlin Heidelberg, Berlin, Heidelberg, 1999, pp. 9–18, https://doi.org/10.1007/978-3-642-60041-8_2.

[53] B.P. Barbero, J.A. Gamboa, L.E. Cadús, Synthesis and characterisation of La1−xCaxFeO3 perovskite-type oxide catalysts for total oxidation of volatile organic

compounds, Appl. Catal. B 65 (2006) 21–30, https://doi.org/10.1016/J.APCATB.2005.11.018.

[54] S.Q. Chen, H. Wang, Y. Liu, Perovskite La–St–Fe–O (St=ca, Sr) supported nickel catalysts for steam reforming of ethanol: the effect of the a site substitution, Int. J. Hydrog. Energy 34 (2009) 7995–8005, https://doi.org/10.1016/J.IJHYDENE.2009.08.007.

[55] F. Zaza, S. Frangini, J. Leoncini, I. Luisetto, A. Masci, M. Pasquali, S. Tuti, Temperature-independent sensors based on perovskite-type oxides, J. Appl. Phys. (2014) 53–61, https://doi.org/10.1063/1.4883042.

[56] I. Popescu, M. Piumetti, S. Bensaid, I.C. Marcu, Study of Ce-cu mixed oxide catalysts by: in situ electrical conductivity measurements, Phys. Chem. Chem. Phys. 19 (2017) 31929–31939, https://doi.org/10.1039/c7cp04517d.

[57] G.E.E. Gardes, G.M. Pajonk, S.J. Teichner, Catalytic demonstration of hydrogen spillover from nickel-alumina catalyst to alumina, J. Catal. 33 (1974) 145–148, https://doi.org/10.1016/0021-9517(74)90255-3.

[58] M. Lo Faro, V. Antonucci, P.L. Antonucci, A.S. Aricó, Fuel flexibility: a key challenge for SOFC technology, Fuel 102 (2012) 554–559, https://doi.org/10.1016/J.FUEL.2012.07.031.

[59] M. Lo Faro, A.S. Aricò, Electrochemical behaviour of an all-perovskite-based intermediate temperature solid oxide fuel cell, Int. J. Hydrog. Energy 38 (2013) 14773–14778, https://doi.org/10.1016/j.ijhydene.2013.08.122.

[60] M. Lo Faro, V. Modafferi, P. Frontera, P. Antonucci, A.S. Aricò, Catalytic behavior of Ni-modified perovskite and doped ceria composite catalyst for the conversion of

odorized propane to syngas, Fuel Process. Technol. 113 (2013) 28–33, https://doi.org/10.1016/j.fuproc.2013.03.010.

[61] R. Baruah, M. Dixit, P. Basarkar, D. Parikh, A. Bhargav, Advances in ethanol autothermal reforming, Renew. Sust. Energ. Rev. 51 (2015) 1345–1353, https://doi.org/10.1016/J.RSER.2015.07.060.

[62] N.R. Peela, D. Kunzru, Oxidative steam reforming of ethanol over Rh based catalysts in a micro-channel reactor, Int. J. Hydrog. Energy 36 (2011) 3384–3396, https://doi.org/10.1016/J.IJHYDENE.2010.12.091.

[63] X. Han, Y. Yu, H. He, W. Shan, Hydrogen production from oxidative steam reforming of ethanol over rhodium catalysts supported on Ce–La solid solution, Int. J. Hydrog. Energy 38 (2013) 10293–10304, https://doi.org/10.1016/J.IJHYDENE.2013.05.137.

[64] A.C. Furtado, C.G. Alonso, M.P. Cantão, N.R.C. Fernandes-Machado, Support influence on Ni–cu catalysts behavior under ethanol oxidative reforming reaction, Int. J. Hydrog. Energy 36 (2011) 9653–9662, https://doi.org/10.1016/J.IJHYDENE.2011.05.063.

[65] M. Giuliano, M.C. Valsania, P. Ticali, E. Sartoretti, S. Morandi, S. Bensaid, G. Ricchiardi, M. Sgroi, Characterization of the evolution of noble metal particles in a commercial three-way catalyst: correlation between real and simulated ageing, Catalysts 11 (2021) 247, https://doi.org/10.3390/CATAL11020247.

[66] A. Gallo, C. Pirovano, P. Ferrini, M. Marelli, R. Psaro, S. Santangelo, G. Faggio, V. Dal Santo, Influence of reaction parameters on the activity of ruthenium based catalysts for glycerol steam reforming, Appl. Catal. B 121–122 (2012) 40–49, https://doi.org/10.1016/J.APCATB.2012.03.013.